DEVELOPMENT OF A PATIENT-SPECIFIC DEFORMABLE IMAGE REGISTRATION MODEL FOR BREASTS USING POSITRON EMISSION TOMOGRAPHY COMBINED WITH MAGNETIC RESONANCE IMAGING BY BIOMECHANICAL STRATEGY

XUE CHENG

Ph.D

The Hong Kong Polytechnic University

2017

The Hong Kong Polytechnic University

Department of Health Technology and Informatics

Development of a Patient-specific Deformable Image Registration Model for Breasts Using Positron Emission Tomography Combined with Magnetic Resonance Imaging by Biomechanical Strategy

XUE Cheng

A thesis submitted in partial fulfilment of the requirements for the degree of Doctor of Philosophy

August 2016

CERTIFICATE OF ORIGINALITY

I hereby declare that this thesis is my own work and that, to the best of my knowledge and belief, it reproduces no material previously published or written, nor material that has been accepted for the award of any other degree or diploma, except where due acknowledgement has been made in the text.

____________________________ (Signed)

Cheng Xue (Name of student)

Abstract

The simulation of large deformations of the breast has great potential for applications in the medical field, such as breast cancer diagnosis, image guided surgery, surgery planning and breast image registration. However, the positioning of the patient body will differ during each screening modality. Large-scale deformations of the breast during movement mean that modeling of the breast is a difficult task. It is therefore necessary to formulate a mechanical model of the breast that can predict the deformations of the breast during scanning.

In this thesis, I propose an individualized biomechanical model to predict large-scale deformations of the breast in the supine to prone positions. The model combines finite element analysis with affine transformation. The mechanical properties of the breast tissues are individually assigned by using an optimization process, which allows the model to be patient-specific.

Image registration with the use of positron emission tomography (PET) and magnetic resonance imaging (MRI) has been extensively studied in the literature. The biomechanical model of the breast is thus evaluated by using MRI and PET/computed tomography images from Hong Kong and American samples. The differences in the breast volume and density are determined by the biomechanical model in this study. Deformations in the breast images of both the Asian and American samples due to the effect of gravity are successfully modeled by using the finite element method.

The accuracy of the developed model is determined by using the target registration error (TRE) of the lesion. The TRE for the Hong Kong and American samples is 4.77±2.20 mm and 8.40±7.15 mm, respectively. The results show that this model is

able to accurately predict deformations of the breast in the supine to prone positions for images from both populations.

In addition, the TRE has been found to be correlated with the image density, which indicates that this model can more accurately predict deformations of breasts with less density. A decision tree has also been generated through data mining to predict the registration accuracy.

Publications arising from the thesis

Submitted journal paper:

1. **Cheng Xue**, Fuk-Hay Tang, Zhong-Jun Mo, Christopher W.K. Lai, "A patient-specific biomechanical image registration model for the breast using positron emission tomography and magnetic resonance imaging", submitted to Medical engineering & physics.
2. Winnie Wai-Ying Kam; **Cheng Xue**; Lau Lai-Yee; Benjamin Y.M. Yunga; Richard B. Banatib. "Dose and time dependent radiation effects in human mitochondria: study from DNA, mRNA and morphology perspectives", Submitted.
3. **Cheng Xue**, Fuk-Hay Tang, Joseph Y. Lo, Christopher W.K. Lai, "Modelling breast deformation of ethnically different women with biomechanical model", submitted to IEEE transations on medical imaging.

EI indexed conference paper

4. **Xue, Cheng**, Tang, Fuk-Hay. (2014). " An adaptive patient specific deformable registration for breast images of positron emission tomography and magnetic resonance imaging using finite element approach", Proc. SPIE 9034, Medical Imaging 2014: Image Processing, 90343H (March 21, 2014); doi:10.1117/12.2043252;

International conference papers

5. **Xue C**, Tang FH. "A patient specific image registration breast model for PET/MRI". In: Proceeding of the 6th WACBE World Congress on Bioengineering. p496. Beijing China. Aug 5-8, 2013.

6. **Xue C**, Tang FH, Christopher W.K. Lai. “A breast registration model based on finite element analysis for positron emission tomography and magnetic resonance imaging” 20th Asia-Australasia Conference of Radiological Technologists, 2015.

Book Chapter

7. **Cheng Xue**, “Finite element analysis in medical imaging”. Recent Advances in Imaging, in preparation.

Acknowledgements

First, my appreciation must be extended to my chief supervisor, Dr. Fuk Hay Tang, for his excellent guidance, patience and immense knowledge, and for providing me with the invaluable opportunity to pursue my Ph.D. degree. His endless support has helped me at all times during the research and writing of the thesis. His hard-working attitude and immense enthusiasm towards research have impressed me very much. I would also like to thank my co-supervisor, Dr. Christopher Lai, for obtaining images from the local hospital for this study as part of my research and also guiding my research for the past several years.

I would also like to express my deepest gratitude to my mentor at Duke University, Prof Joseph Lo, for his support and brilliant ideas, as well as his supervision during my stay, my colleague Yuese Zheng, Brian Harrawood, Greg Sturgeon and all of the members of the Carl E. Ravin advanced imaging laboratories. Their passion really inspired me, and I really appreciated the time that I spent in the lab.

My sincere gratitude also goes to all of my colleagues in Hong Kong, especially every one of my officemates in Y607 and other friends, especially Dan Chong, Enna Ha, Zhuoming Chen, Wei Zheng and Xiao Li. The past four years were so much better with all of them. I would like to give special thanks to Da Chen, for his patience and consolation on the phone every night. Gratitude also goes to the University of Cambridge/Department of Engineering, for the mechanical properties information posted on their website.

Finally, I am indebted to my family for their unconditional love and tremendous amount of support throughout my Ph.D. study and their Facetime with me whenever I missed them.

Contents

List of Figures

List of Tables

1 Introduction

1.1 *Background information*

About one in eight women will develop breast cancer over the course of their lifetime. The treatment for breast cancer is to surgically remove the lesion(s) and some of the healthy tissue around the lesion(s). It is vital to identify the location of the cancer lesion(s) before and during surgery. Therefore, the patient will undergo medical image scanning prior to surgery. Registered medical images can provide clinically combined information from different imaging modalities. However, the positioning of the body of the patients will not be the same during each scan. Therefore, a biomechanical model that can simulate the movement of breasts to track the lesion(s) is greatly needed.

Since the early diagnosis of breast cancer is also very important, molecular imaging such as positron emission tomography (PET) can detect the lesion(s) in the very early stages, but provides limited spatial information. Therefore, PET and magnetic resonance imaging (MRI) are used together to provide images with more detailed information. The PET image is usually taken in the supine position, and MR image in the prone position. A realistic biomechanical model can finish the registration of PET and MR images by predicting the deformations of the breasts in the supine to the prone positions.

Finite element analysis (FEA) is widely used in engineering, such as civil and mechanical engineering. It is a numerical means for finding solutions to complicated problems. The highlight of using FEA is that the technique allows researchers to simulate various practical problems or physical situations, such as stress analysis for simply supported beams, heat transfer, and deformation of various materials. In addition, FEA plays a dominant role in biomechanics, by which researchers can analyze the stress and strain of bonds under particular loading environments.

This thesis endeavors to develop a technique to predict soft tissue movement. The primary clinical goal is to formulate a biomechanical model that can simulate the deformations of the breasts in the supine to prone positions, and register MR and PET images together to improve early diagnosis of breast cancer. It is anticipated that this model can also assist with image-guided breast surgery and therapy planning.

1.2 *Key contributions*

In this study, FEA is applied to formulate a biomechanical model of the breast. The model is validated by finishing the registration of MR and PET breast images, as image registration is very important for the diagnosis of breast cancer. Therefore, a hybrid PET/MR image registration model is established. The advantage of integrating FEA into a registration method is to obtain a high level of correlation with the material properties, which means that this FEA model is specific to the individual.

This registration model which is based on FEA will take into consideration material properties. An inverse FEA is also conducted to noninvasively measure the tissue properties. This ability to noninvasively measure material property is quite useful in clinical settings.

The established model is evaluated by using images from two countries. A correlation between density and accuracy is found. The registration accuracy can be predicted with nipple displacement and density before conducting the registration process.

1.3 *Thesis Structure*

The components of this dissertation are organized into a flowchart and shown in Figure 1.1.

As the first step, the FEA is customized for biomedical purposes. Then, the theoretical details and background will be provided in Chapter 2. Related studies will also reviewed in this chapter.

Chapters 3 to 5 include discussions on the development of patient specific FEA models and evaluation of their clinical applications. There are three major tasks: building of a biomechanical model, simulating of deformation under gravity, and evaluation.

In Chapter 3, the features that need to be taken into consideration will be discussed. The influence of skin will be assessed to determine whether the modeling of skin is necessary. The method used to determine the reference state, mesh density and element shape will be provided. The Poisson's ratio that represents the volume change of objects will also be determined. Finally, the process for processing images will be described.

In Chapter 4, an FEA model that can simulate breast deformations from the supine to prone positions will be introduced. Since the mechanical properties greatly affect deformations in FEA, and every woman has her own mechanical properties, these properties also vary when metastasis takes place. Therefore, in this study, a biomechanical model of the breast that takes tissue properties into consideration will be formulated. As well, an evaluation method for examining deformed PET images is critical. PET images have a very low resolution. It is not possible to identify enough landmarks for evaluation purposes. Therefore, an evaluation system for PET/MR image registration is also proposed in this study.

In Chapter 5, I will use 28 sets of PET/ computed tomography (CT) and MR images from two different countries to further evaluate the breast model for the supine-prone positions. I will determine a correlation between model accuracy and image features. Data mining is also used to predict the registration accuracy. Chapter 6 will provide an overall conclusion and recommendations for future studies.

This thesis will demonstrate that the developed individualized biomechanical model can predict deformations of the breast and accurately track the location of lesion(s) .

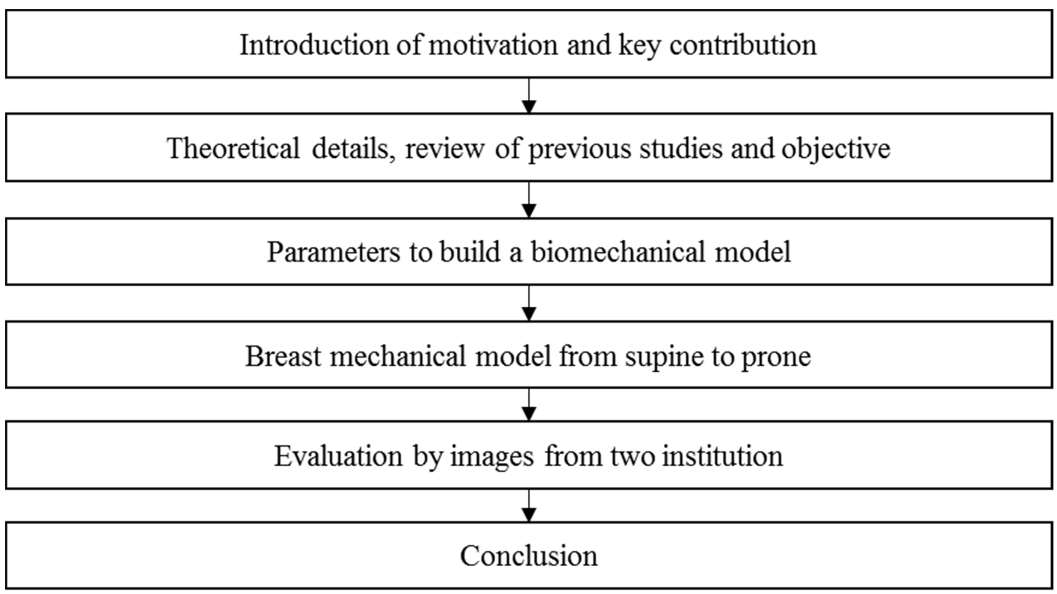

Figure 1.1 Thesis components.

2 Literature review

2.1 ***Breast imaging, breast anatomy and image registration***

2.1.1 Breast anatomy

The mechanics of breasts vary due to their structure and the different mechanical properties of their constituents. In order to simulate breast deformations under different loading environments, a brief understanding of the breast anatomy is necessary. In this section, a general introduction on the anatomical structure of the breast will be provided.

The classical definition of the female breast is restricted to the anterior and lateral parts of the chest, and the superior and inferior margins between the second to sixth or seventh ribs. Typically, breasts are teardrop shaped, with the axillary tail extending up to the mid-axillary line.

The breast components can be classified as external and internal. External components include the nipples, areolas, tubercles and some glands. Internal components consist of three major types of tissues: glandular, fat and fibrous, as shown in Figure 2.1. The glandular tissues of breasts are made up of 15-20 lobes that produce milk. The lobes consist of smaller components of fibrous walls, which are called lobules. There is a network of ducts that connects the lobules and nipples. These ducts are very tiny ductules at the beginning across the lobules, but become larger and larger when they approach the region near the nipples. The ducts and lobules are held in place by the fibrous tissues. The glandular and fibrous tissues are also known as fibro-glandular tissue. The fibro-glandular tissues are surrounded by fatty or adipose tissue. Depending on their age or even pathological changes, women have different proportions of fibro-glandular to fatty tissue. Fatty tissue always accounts for a large proportion or at least one third of the breast tissue. Menopause also affects the mass of these two types of tissues because it will lead to the atrophy of the fibro-glandular tissues, which will result in a greater proportion of adipose to fibro-glandular tissue.

When it comes to the mechanics of the breasts, Cooper's ligaments play an important role in helping with the structural integrity of the breasts (Cooper, 1840). Cooper's ligaments are connective tissues that hold the entire breast, and if these ligaments stretch, the breasts will sag. There is a large muscle beneath the breast which is called the pectoralis major (pectoral muscle), which separates the breast from the rest of the body.

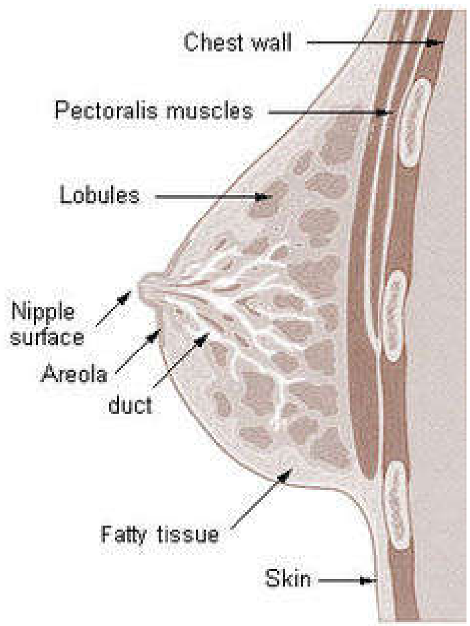

Figure 2.1 Structure of the breast. (Source:(New World Encyclopedia, 2008)) .

2.1.2 Breast cancer imaging

Breast cancer is the second most prevalent type of death causing cancer in women after lung cancer. Once diagnosed with breast cancer, the quality of life of the patient will be severely affected. The risk of developing breast cancer depends on many factors, including age, personal or family history of breast cancer, parity, age at first birth and use of hormonal replacements. Since over 70% of the breast cancer cases do not have any identifiable risk factors, the early diagnosis of breast cancer is of utmost importance.

According to a 2014 publication on cancer facts and figures in the United States (American Cancer Society, 2014), the most common type of cancer is prostate cancer, with more than 238,000 new anticipated cases. The next most common type of cancer is breast cancer, with more than 232,340 anticipated new cases (Table 2.1).

Table 2.1. Estimated new cases of cancer and related deaths in the US: 2013.

Cancer Type	Estimated New Cases	Estimated Deaths
Bladder	72,570	15,210
Breast (Female – Male)	232,340 – 2,240	39,620 – 410
Colon and Rectal (Combined)	142,820	50,830
Endometrial	49,560	8,190
Kidney (Renal Cell) Cancer	59,938	12,586
Leukemia (All Types)	48,610	23,720
Lung (Including Bronchus)	228,190	159,480
Melanoma	76,690	9,480
Prostate	238,590	29,720

The most common used types of screenings for breast imaging are x-ray mammography, ultrasound, contrast-enhanced MRI (CE-MRI), and CT.

Mammography is a diagnostic and screening tool which uses low energy x-rays to take images of the breasts. Breast cancer is detected with the development of characteristic masses and microcalcifications in the breast tissue. The sensitivity of mammography ranges from 83% to 95% (Mushlin et al., 1998).

In the ultrasound process, ultrasound waves that are transmitted by using a probe, interact with the tissue. When these waves hit the interface of materials with different mechanical impedance, they are either absorbed or reflected back to the probe. Different materials can be distinguished based on the different amplitudes of the echoes. Breast ultrasound is performed on patients to further investigate suspicious lesions found during mammography, or from lumps felt in the breast by the patient herself during self examination or a physical examination.

CT scanning is an x-ray technique that gives doctors information on the internal organs in 2-dimensional slices, or cross-sections. Currently, CT scans are not routinely used to examine the breasts. However, doctors may use CT scanning to assess whether cancer has spread into the chest wall.

MRI is a diagnostic procedure which uses magnetic fields, radio waves, and field gradients along with a computer produces detailed images of the organs and structure of the body. To implement breast MRI, the female patient usually lies face down with her breasts positioned through an opening in the table.

2.1.3 Need for better imaging tool to diagnose breast cancer

Approximately 12% of women will face breast cancer in their lifetime. In the US, about 3.5 million women have had a history of invasive breast cancer (American

Cancer Society, 2016b). Furthermore, 246,660 new cases are estimated for 2016 (American Cancer Society, 2016b). Breast cancer can be effectively treated when detected at the early stages, and the prognosis heavily depends on the tumor size (Brinkley & Haybittle, 1975). When a suspicious lesion is detected, a biopsy is carried out to confirm the presence of cancer and the stage (Mendez et al., 2004).

Although breast biopsy is a highly specific and sensitive test for the diagnosis of breast cancer, it is invasive and will leave a scar that will affect future breast examinations. Moreover, biopsy has a relatively high false negative rate around 50%, probably due to technical errors and the inexperience of medical practitioners (Moskowitz, 1995). Therefore, it would be ideal to have other non-invasive imaging techniques in place for follow up with an occult breast lesion. Although there are different imaging modalities used to detect breast cancer, there are pros and cons when they are applied to detect breast cancer, as follows.

2.1.3.1 X-ray mammography

X-ray mammography is the main technique used to detect and diagnose breast malignancies (Moskowitz, 1995). The superimposition of breast tissue and parenchymal density, this limitation can obscure cancers or make normal structures appear suspicious. This shortcoming can reduces the sensitivity and increase the false-positive screening of mammography (Ciatto et al., 2013). These shortcomings have thus led to the investigation of alternative imaging modalities, such as ultrasound (Harper et al., 1981; Wu & Moon, 2008), MRI (Moskowitz, 1995; Orel & Schnall, 2001), CT (Boone & Lindfors, 2006), PET (Avril et al., 2000), and single-photon-emission computed tomography (SPECT) (Wendler et al., 2010), for the detection and diagnosis of breast cancer.

2.1.3.2 Positron emission tomography

PET is a type of molecular imaging modality that can reflect the metabolic pathways and dynamic processes in vivo. This technology can recognize breast cancer at the molecular level for an early diagnosis and prompt treatment. PET is sensitive and informative in the processing of diseases that are biological in nature. Measurements can be repeated many times during the day by using isotope with long half-life, because there is less radiation, due to the shorter half-life radiotracers which are commonly used in nuclear medicine and therefore PET scanning. The accuracy of PET diagnosis is 8 – 43% higher than that of the CT, mammography and other techniques (Phelps, 2000). However, the localization of potential tumors is very difficult due to low spatial resolution of the PET images and limited anatomical information obtained (Antoch & Bockisch, 2009).

2.1.3.3 Magnetic Resonance Imaging and Computed Tomography

MRI and CT are both morphological imaging modalities that reveal the structure of tumors or organs. However, because both techniques only provide morphological information, there is not enough functional information (Haberkorn & Schoenberg, 2001).

2.1.3.4 PET/MR imaging

Different breast imaging modalities provide complementary information that can help to make a diagnosis or assist the clinician for a therapeutic gesture. Image registration obtained by the imaging modalities comprises inter-modality and intra-modality registration. In this thesis, the focus will be on inter-modality image registration. Researchers have been working on inter-modality breast image registration for a long time. The modalities involved are x-ray mammography, MRI and ultrasound imaging. The registration of x-ray mammograms is a 2-D/2-D problem, while that of MRI and ultrasound imaging is a 3-D/3-D problem.

The inter-modality breast image registration techniques include: x-ray mammography and MRI registration, MRI and ultrasonography registration, PET and CT registration, PET and MRI registration, and X-ray mammography and ultrasonograph registration (Guo et al., 2006).

Therefore, to enhance the image quality of PET, a registration process needs to be developed which can fuse PET images with another imaging modality. Efforts have been made to combine PET with CT to make use of the CT for attenuation correction, a major signal degradation in nuclear medicine imaging, and anatomical reference. These efforts aim to increase the resolution of the images in clinical practice. As a result, a multi-modality imaging system for clinical settings has been developed to fill the need. But the resolution of CT image for soft tissue is less than MRI.

For over a decade, PET/CT as a multi-modal imaging technology has had great achievements in both scientific research and clinical settings. However, as MRI excels CT in many aspects, research on MRI has been more prevalent in recent years. Therefore, a combined PET/MRI scanner can significantly change health care and revolutionize clinical practice. This combined scanner excels the traditional PET/CT scanner, as the differentiation of soft-tissue can be contrasted. Also additional function information of MR image can be applied to PET/MRI registered image, and radiation of MRI is less than CT.

F-18-FDG PET and MRI are both well-proven methods for breast cancer detection in their own right. MRI provides high sensitivity (95–99%) and various specificities

(50–92%), while F-18-FDG-PET demonstrates various sensitivities (63–95%) and high specificities (80–95%) (Moy et al., 2007). Therefore, it is reasonable to infer that combining F-18-FDG PET with MRI and perhaps with some other non-invasive breast examination methods (e.g. Breast SPECT imaging system or magnetic resonance spectroscopy) will constitute as significant methods for diagnosing breast cancer.

The advantages to combining these different imaging methods could provide sufficient diagnostic specificities to reduce unnecessary breast biopsies with a set of non-invasive imaging procedures. Indeed, Rieber et al. (Rieber et al., 2002) noted that in doing so, this positively affects surgical treatment in 12.5–15% of the cases studied. Walter et al. reported that the combined use of F-18-FDG PET and MRI retrospectively reduces unnecessary biopsies from 55% to 17%(Walter et al., 2003). Moy et al. reported that the use of both PET and MRI to generate breast images increases the specificity (from 2% to 95%) but decreases the sensitivity (from 92% to 63%) when compared to the use of MRI alone(Moy et al., 2007).

The combined use of PET and MRI can also provide clinicians with the opportunity to obtain both structural information and structural data in vivo, which are more specific than the image attained from a single imaging modality (Solis et al., 2010).

However, although PET/MRI scanning has great potential, but this combined method is time consuming, expensive, and logistically demanding of patients and staff. As well, patient repositioning can cause inaccurate anatomic matching and side-by-side interpretation of images results in diagnostic inaccuracies.

Nevertheless, MRI, on its own merits, is an imaging technology that can clearly reflect the anatomical structure. Since patients may not be able to undergo PET and MRI scanning at the same time, hence, registration of PET and MRI is still necessary.

2.1.4 Registration

2.1.4.1 Image registration methods

The goal of image registration is to determine the Euclidean motion between a set of images of a given object taken from different locations in order to represent them all with respect to a reference frame. Image registration is defined as spatial mapping between two images (Guo et al., 2006). Usually, image registration is classified into rigid registration and non-rigid registration, as shown in Figure 2.2. Non-rigid registration is the most suitable method for breasts. To achieve non-rigid registration, the deformable image registration (DIR) method can be used followed by using an FEA to build a mechanical model for predicting the deformation of organs and tissues with two parameters: boundary conditions and meshing.

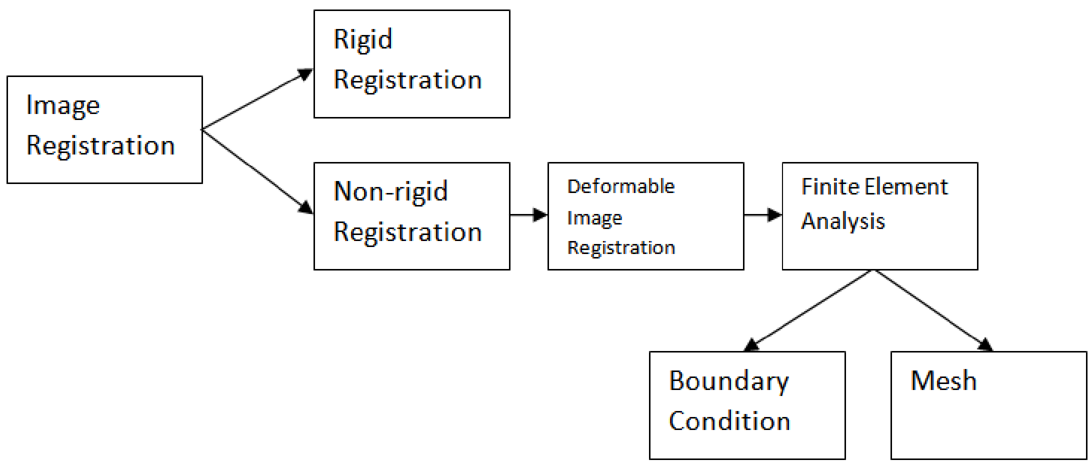

Figure 2.2. Types of image registration.

2.1.4.2 Limitations of image registration: rigid registration of breast images

Images can be registered through rigid registration where images are assumed to be objects that simply need to be rotated and translated with one another to achieve symmetry, or non-rigid registration where either through biological differences or image acquisition or both, correspondence between the structures in two images cannot be achieved without some localized stretching of the images.

A number of the previous works on medical imaging registration registered brain images of the same subject taken with different modalities, such as MRI and CT or PET (Hill et al., 1991). For this purpose, rigid body approximation is sufficient, as there are merely slight alterations in brain shape or locations on the skull over the relatively short periods of time between scans. Today, rigid registration is often extended to include affine transformation, which includes scale factors and a number of shears, and can partially correct for the calibration differences across scanners or gross differences in scale between different subjects. Several studies have reviewed these areas in more detail (Hill et al., 2001). Clearly, the human body mostly does not conform to a rigid or even an affine approximation (Hawkes, 1998) and the most interesting and challenging work in registration today involves the development of non-rigid registration techniques for soft-tissue deformation during imaging or surgery (Crum et al., 2014).

2.1.4.3 Deformable image registration

Apart from accuracy and efficiency, image registration techniques need to incorporate deformable alignment, allow various regions of interest to behave differently, and maintain the geometric integrity of inter structures that are different in different imaging modalities. Deformable models have been used to predict the mechanical deformations of tissues or organs based on biomechanical tissue properties and perform non-rigid image registration. They include brain-shift modelling (Ferrant et al., 2001); heart-kinetics modelling (Sermesant et al., 2006); breast-compression simulation, such as in x-ray mammography (Richard et al., 2006); and breast-image registration (Roose et al., 2006).

As pre-treatment imaging becomes increasingly integrated into the treatment planning process and full three dimensional (3D) image guidance becomes part of the treatment delivery, demand for a DIR technique becomes more apparent.

Currently, DIR comprises two categories, image-based DIR and physics-model-based DIR. For the former, image information like landmarks and intensities has been used to locate the best voxel match between two images. It is an optimization problem that searches for a point-wise transformation, thus minimizing discrepancies between two data sets to be matched by using global voxel-based similarity metrics. In terms of biomechanical tissue properties, physics-based DIR has been applied to obtain advanced information on the mechanical deformations of tissues or organs. Thus non-rigid image registration is possible (Unlu et al., 2010). For the latter, image registration can use FEA. As organs are often considered to be elastic objects, FEA can be used to study their deformation.

2.1.5 Supine to prone position registration

Prone MRI and supine PET/CT are usually applied due to different consideration in using either one imaging. Therefore, there is a question, if know advance for required use of both imaging, supine MRI or prone PET/CT be applied in order to avoid the huge deformation difference. However, the PET and MR scan are not conducted simultaneously. Even the huge deformation of breast is avoid, there is still body movement between this two scanning. Breath will also cause difference of breast shape. This difference caused by different pose and breast is harder to simulate.

Registration of PET image in supine position and MRI in prone position can provide bias for retrospective study, also reverse finite element analysis can be used to estimate the mechanical properties of breast.

2.2 *Computer aided detection*

Biopsies have been considered as the golden standard for breast cancer diagnosis, but is a very painful process. Approximately 2/3 of the breast lumps turn out to be benign after a biopsy is performed. However, both early detection and the true positive rate of biopsies are related to the experience of radiologists. Radiologists are involved in radiology, reading images of mammograms and undertaking assessment clinics (Astley & Gilbert, 2004).

Sometimes breast cancer signs can be ambiguous or even undetectable by radiologists, which may lead to misdiagnoses, such as by mistaking malignancy as benign. However, excessive attention to details in the original screening is time costly, thus leading to reductions in efficiency. Actually, the signs of breast cancer are overlooked in about 10-30% of the patients during routine screening (Cheng et al., 2003).

Uncertainty is also very common in clinical practices, which means that patients who are suspected of having signs of breast cancer undergo a painful biopsy, but in fact, the tumor is benign. Hence, this is a waste of resources and human labor.

These situations take place due to the radiologists. In mammographic film reading, radiologists are responsible for all of the details and symptoms found in the screening. The signs are often hard to detect and tumors do not have a regular shape. To overcome the difficulties in mammographic film reading, a double reading is recommended. Consequently, false-negative rates can be greatly reduced. Sometimes a third reader is necessary to make a decision when two readers cannot reach an agreement. This process will ensure the quality of the breast cancer diagnosis; however, the number of experienced radiologists is limited, so that double reading or using a third reader is likely to be only possible when there are adequate radiologists available. Even if there is the desire to use double reading, experienced radiologists are very limited in comparison to the increasing number of patients.

Computer aided detection (CAD) has been regarded as an alternative method to solve the labor shortage problem of radiologists. The current situation is that, on the one hand, many screening centers do not have a sufficient pool of radiologists to perform double reading of all the films. On the other hand, the difficulty also comes from a larger screening population and changes in screening practices. It is difficult for radiologists to provide both accurate and uniform evaluations for the increasingly large numbers of mammograms due to widespread screening.

One possible solution is to computerize the process in clinical practices so as to detect abnormalities in images. As computerized processes are highly efficient, the shortage of labor then becomes a non-issue.

CAD was developed to assist radiologists to carry out diagnosis as routine practices, and has been applied to different screening processes, such as that for lung cancer, and cervical and mammogram screening.

The task of medical image interpretation is to seek abnormal lesions, then describe their characteristics. Then radiologists can diagnose based on these characteristics. CAD means that computers can assist in detecting abnormalities and characterizing lesions. Lesions also change over time, so CAD can also be used to monitor the changes.

The most common sequence of the CAD process is: detection, description, diagnosis and prognosis. All four steps have corresponding systems, which are as follows.

Detection

In terms of detection, the function is to identify abnormal signals that could be unnormal in an image. For example, the identification of suspicious micro calcifications in mammograms, or detection of colonic polyps in CT colonographies. Detection is usually used as a means of prompting, and thus suspected abnormalities are located by overlaying a medical image.

Characterization/description

Computer aided characterization (CAC) is designed to provide specific descriptions of lesions in a medical image. These descriptions should be renewable and accurate. This is when there is the need to evaluate some data sets that should be processed more than once during a period of time, such as the detection of enhanced characteristics of a breast nodule on MRI.

Diagnosis

The aim of computer-aided diagnosis (CADx) is to accurately describe a disease, especially the likelihood of a particular disease. An example is that in mammography, CADx can recognize clusters of microcalcifications based on criteria that have been previously determined, and then the probability of a malignant lesion will be provided. This helps radiologists to make a decision on whether the patient should undergo a tissue biopsy for further confirmation. There are limitations in the use of CADx in clinical practices because even if an abnormal lesion is detected, the number of potential diseases related to this lesion is limited.

Prognosis

The aim of computer-aided change detection (CACD) is to identify sequential changes in a specific region. For instance, comparison of the changes in a lesion after diagnosis. The CACD system is able to quantity the changes and determine the magnitude of the changes after diagnosis. Actually, CACD systems do not replace physicians. Instead, they can work as a tool for physicians, and help them to make a more informed decision. The advantage of CACD systems is that they can combine the clinical experiences of radiologists with the computational power of computers, which can lead to a reduction in time required to read an image and variability in different observations will also decrease. The common procedure for carrying out CACD is as follows. First, digital images are acquired. Then some of the features will be extracted from the images. Finally, a clinical decision will be made based on the classified features.

Feature classification includes the use of pattern recognition neural networks and information modeling to obtain a usable output, such as the likelihood of malignancy and differential diagnoses, from analyzing the features (Kagadis & Langer, 2011). This step mimics the work of a radiologist to recognize particular patterns and analyze their relationship with different diseases. To finish this process, commonly used methods include statistical methods and use of neural networks, so as to process large amounts of data, including numerous medical information. The accuracy of the diagnosis not only depends on the information in the images, but also takes into consideration the medical context of the patient who underwent the imaging to include all the diseases that are possible. When CACD is utilized in the image interpretation process by a physician, it can be applied either as a first, second or concurrent reader, but second reader is more common.

Researchers have developed numerous algorithms to detect abnormalities in mammographs for a long time. CACD systems were initially developed to replace radiologists, but much evidence has shown that this cannot be done. It is easy for a computer to extract features but difficult to make the judgment between benign and malignant as opposed to radiologists, who diagnose based on their experience. Nevertheless, CACD can be a supplementary tool for radiologists, due to its strong operational ability to analyze a large number of images without being tired. CACD systems can help to draw the attention of the film reader to suspicious areas (Kagadis & Langer, 2011).

2.2.1 Challenge of building PET/MR image registration model of human breasts

Breast images acquired at different times, or with different imaging modalities are often registered to help with the analysis or visualization of image. Image registration is widely used in many applications, such as for better visualization of lesions and combining breast images obtained from different modalities. The inhomogeneous, anisotropic nature of the soft-tissue in the breasts, their inherent non-rigid body behavior, the temporal changes in breast tissue, and various imaging conditions, render breast image registration a challenging task (Guo et al., 2006).

Due to differences in the resolution obtained through PET and MRI, as well as large differences in the image formation processes, imaging intensity relationships in PET and MRI are ill defined. Therefore, such techniques, which rely on similarity measures, generally provide unsatisfactory results for non-rigid MR-to-PET registration of soft tissue.

Accurate 3D registration and overlay of MR and PET images of the breast could provide important additional information by connecting functional information from PET images with the detailed anatomical information available in the MR images (Studholme et al., 1997). Interactive methods based on user guided registration or user identification of landmarks are robust but time consuming, require observer skills and therefore rely on observer bias or error.

In addition, variations in the image resolution and patient orientation can mean that the combining of image information is difficult for clinicians. To solve this problem, considerable research work has been conducted that use image registration techniques to combine images from different imaging modalities into one coordinate (Studholme et al., 1996).

The existing registration method is very time-consuming which would affect the early diagnosis of breast cancer. Overprocessing of images can mean the loss of specific clinical features, and lead to inaccuracy of registration and later diagnosis and treatment. In this study, a registration method will be established for PET and MRI, which will reflect the specific features of patients, reduce the computation time and increase accuracy. The modeling process is completed by using commercial software, so that the whole process is more convenient and more adaptable for clinical diagnosis.

2.3 *Finite elasticity theory*

In recent years, there has been growing interest in using FEA for the modeling of the behavior of biological systems. The breasts consist of soft tissues, and are one of the most deformable organs in the human body. Deformations under gravity and compression are considered to be large deformations. Therefore, to examine these deformations, a theory of large elastic deformations, and the finite elasticity theory which is also known as the nonlinear elasticity theory will be used. The elasticity theory is based on the concepts of stress, which is a measure of internal pressure; and strain, which is a measure of internal stretching. Four key relations need to be considered for the simulation of large deformations of the breast: kinematics, stress equilibrium, boundary conditions and constitutive relations.

2.3.1 Constitutive relations

Constitutive relations are a mathematical relationship that can define the relationship between stress and strain. The form of the constitutive relation is based on specific material behavior, rather than a general relationship. The focus is on determining how particular materials behave under specific conditions. To identify the relationships, the modality of the body of interest, such as a solid, fluid or mixture, needs to be decided. For a solid body, the material could be elastic/ inelastic, isotropic/ anisotropic, linear/nonlinear, and homogeneous/ heterogeneous. The following is a brief introduction on some of the universal characteristics.

Isotropic: Isotropic bodies respond to loading only relative to a prescribed configuration, and not the direction of loading. There is also a type of isotropic material that only responds to a single direction of loading, which is known as transversely isotropic material.

Orthotropic: Orthotropic materials only response to loading in three orthogonal directions.

Homogeneous: The response of homogenous bodies should be the same, regardless where the loading is applied on the body.

Heterogeneous: Also known as inhomogeneous bodies, which means that their response will depend on their position.

Incompressible: The volume of an incompressible body remains constant in loading conditions. (Humphrey & Rajagopal, 2002) indicated that since most of the tissues in the human body contain plenty of water, tissues are thus almost incompressible.

2.3.2 Boundary conditions

The boundary conditions are the application of a force and/or constraint. They are the specified values of the field variables on the boundaries of the field. Typically, there are two kinds of boundary conditions: loads and constraints. Loads include forces, moments, pressures, temperatures, accelerations. Constraints resist the deformations induced by the loads.

2.3.3 Kinematic equations

Kinematic equations represent how a body of interest shifts when it is subjected to loads. In this study, the motion of the breasts under gravity from the supine to prone positions is the focus. The motion of an object from an undeformed state (X) to a deformed configuration (x) can be represented by using the deformation gradient tensor **F**:

$$\boldsymbol{F} = \frac{\partial \boldsymbol{x}}{\partial \boldsymbol{X}} \tag{1}$$

Measurements of the strain in a system can be quantified by using the Green-Lagrange strain tensor (**E**), which is related to the Cauchy-Green deformation tensor (**C**) and the identity tensor (**I**), as:

$$\boldsymbol{E} = \frac{\mathbf{I}}{2(\boldsymbol{C} - 1)} \tag{2}$$

$$\boldsymbol{C} = \boldsymbol{F}^T \boldsymbol{F} \tag{3}$$

2.3.4 Stress tensor for finite elasticity

Stress tensors typically describe when a force is loaded on, and how much force that every unit surface area has endured. Actually, in large deformation mechanics, there are three ways to define stress, because the surface area and force can be measured either in the reference (undeformed) state or current configuration. These three ways are by using a Cauchy stress tensor, and two types of Piola Kirchhoff stress tensors (i.e., the 1st Piola Kirchhoff and 2nd Piola Kirchhoff stress tensors).

2.3.5 Elastic function

In the finite element method, approximation is carried out by using information at each node of a continuous model so that shape deformation can be calculated. This process basically consists of two steps: discretization and interpolation. Discretization is when a structure is divided into many smaller bodies or unites (finite element) interconnected at points common to two or more elements and/or boundary lines and/or surfaces. Interpolation is a process that discrete elements interpolated by shape functions.

The values of the field variables computed at the nodes are used to approximate the values at the non-nodal points by interpolating the nodal values. For the three node triangle, the field variable is described by using the approximate relation:

$$\boldsymbol{\varphi}(x,y) = \boldsymbol{N_1}(x,y)\boldsymbol{\varphi}_1 + \boldsymbol{N_2}(x,y)\boldsymbol{\varphi}_2 + \boldsymbol{N_3}(x,y)\boldsymbol{\varphi}_3 \qquad (4)$$

where $\boldsymbol{\varphi}_1, \boldsymbol{\varphi}_2$ and $\boldsymbol{\varphi}_3$ are the values of the field variable at the nodes, and N_1, N_2 and N_3 are the interpolation functions, also known as the shape or blending functions.

In the FEA, the nodal values of the field variables are treated as unknown constants that need to be determined. The interpolation functions are mostly polynomial forms of the independent variables, derived to satisfy certain required conditions at the nodes.

The interpolation functions are predetermined, and the functions of the independent variables are also known, so these functions will describe the variations in the field variables within finite elements.

2.3.6 Finite Element Model

The FEA is a formidable calculation tool for modeling the deformation of soft tissue. This method has been validated for same-subject non-rigid image registration and anatomical based simulations. In fact, the FEA produces physically reasonable deformations of biomechanical tissue. The FEA can also greatly adapt to shapes and produced with a general computer program. Three-dimensional FE reconstruction has been applied in many areas in medical imaging; for example, to image the prostate, brain and breasts, as well as simulate maxillofacial and liver surgeries. An FE model includes the material properties, geometries, and loadings. Displacement loadings are directly applied onto the surface of organs or the internal point positions.

However, there are two obstacles in using the FEA for the simulation of compression as follows:

(1) FEA often requires a good deal of manual work when a patient-specific anatomical image is required, and

(2) it is difficult to find a suitable FE boundary condition for FEA.

FE models include the material properties of an object and integrate with the underlying geometric model to accurately predict displacements and motion based on applied forces, or recover the loads given nodal displacements. Qiu et al. built two finite models in two different mesh resolutions (Qiu et al., 2004). Different tissue elasticity values, Poisson's ratios and boundary conditions were separately defined in the two models to simulate the influence of these items on the quality of the simulation. In their testing, the breast was assumed to be both linear and non-linear. Also, different finite element solvers were used to perform the analyses. The results showed that the performance of the FEM model is primarily affected by the Poisson's ratio and boundary conditions, rather than the tissue properties, mesh resolution and finite element solver. However, when the models have highly accurate affined boundary conditions, the quality of the FEM model can be influenced less by the Poisson's ratio. However, this test was only conducted on a compression model, rather than gravity-induced deformation models.

2.3.6.1 Consideration of material properties in FEA

The first step toward the use of the FEM is to determine the material properties for the solid model constructed in the previous steps. The modeling of biomechanical tissue has gained considerable interest for various clinical and research applications. According to the literature mentioned before, breasts are composed of biological soft tissues, which are known to be incompressible. As mentioned earlier, the female breast is essentially composed of four structures: lobules or glands, milk ducts, and fatty and connective tissues as shown in Figure 2.1. Most biological tissues have a viscous and an elastic response to external deformations. As the scope of this study is limited to slow deformations, the response of the tissue can be considered entirely due to elastic forces (Azar et al., 2001). All of the tissues in the breast are considered to be isotropic, incompressible and inhomogeneous with nonlinear elastic properties in large deformations. The Young's modulus represents how much a material will deform when a load is applied, and Poisson's ratio expresses how much a material will shrink in one direction when it is stretched in the perpendicular direction. An incompressible material will maintain the volume, so the same volume stretched must be shrunk. Since breast tissues have a nonlinear behavior in large deformations, the Young's modulus (E_n) can be taken as a function of the strain for each tissue:

$$\mathbf{E}_n = \frac{\partial \boldsymbol{\sigma}_n}{\partial \boldsymbol{\varepsilon}_n} = \mathbf{b}_n \mathbf{e}^{m_n \varepsilon_n} \tag{5}$$

where σ_n is the nominal stress for tissue type n,

$\varepsilon_n$is the nominal strain for tissue type n, and

$b_n$and m_n are fit parameters experimentally determined for tissue type n (Azar et al., 2001) .

The dynamics of the elastic body are determined by the following system of partial differential equations:

$$\boldsymbol{\rho}_0 \frac{\partial^2 \mathbf{u}}{\partial t^2} = (\boldsymbol{\lambda} + \boldsymbol{\mu}) \left(\frac{\partial^2 \mathbf{u}}{\partial \mathbf{x}^2} + \frac{\partial^2 \boldsymbol{\nu}}{\partial \mathbf{y}\, \partial \mathbf{x}} + \frac{\partial^2 \boldsymbol{\omega}}{\partial \mathbf{z}\, \partial \mathbf{x}} \right) + \boldsymbol{\mu} \nabla^2 \mathbf{u} + \mathbf{f}_\mathbf{x} \tag{6}$$

$$\boldsymbol{\rho}_0 \frac{\partial^2 \mathbf{v}}{\partial t^2} = (\boldsymbol{\lambda} + \boldsymbol{\mu}) \left(\frac{\partial^2 \mathbf{u}}{\partial \mathbf{y}\, \partial \mathbf{x}} + \frac{\partial^2 \mathbf{v}}{\partial \mathbf{y}^2} + \frac{\partial^2 \boldsymbol{\omega}}{\partial \mathbf{z}\, \partial \mathbf{y}} \right) + \boldsymbol{\mu} \nabla^2 \mathbf{v} + \mathbf{f}_y$$

$$\boldsymbol{\rho}_0 \frac{\partial^2 \boldsymbol{\omega}}{\partial t^2} = (\boldsymbol{\lambda} + \boldsymbol{\mu}) \left(\frac{\partial^2 \mathbf{u}}{\partial \mathbf{z}\, \partial \mathbf{x}} + \frac{\partial^2 \mathbf{v}}{\partial \mathbf{y}\, \partial \mathbf{z}} + \frac{\partial^2 \boldsymbol{\omega}}{\partial \mathbf{z}^2} \right) + \boldsymbol{\mu} \nabla^2 \boldsymbol{\omega} + \mathbf{f}_z$$

where $(\mathbf{u}, \mathbf{v}, \boldsymbol{\omega})$ represents the displacement vector in the Cartesian coordinates,

E represents the Young's modulus,

v represents the Poisson's ratio,

$\mathbf{f}_i$ represents the force field, and

$\boldsymbol{\mu}, \boldsymbol{\lambda}$ are Lamé constants, computed with the two following equations:

$$\boldsymbol{\mu} = \frac{\mathbf{E}}{2(1 + \mathbf{v})} \tag{7}$$

$$\boldsymbol{\lambda} = \frac{\mathrm{v}\mathbf{E}}{(1 + \mathbf{v})(1 - 2\mathbf{v})} \tag{8}$$

Depending on the tissue property, large deformations of biological tissues will have more or less strain hardening. In order to describe the deformation that is in response to an external solicitation, a tissue can be considered as an isotropic and linear continuous elastic medium. In this case, the relation between strain and stress can be expressed with tensor notation:

$$\boldsymbol{\sigma}_{\mathbf{ij}} = 2\mu \boldsymbol{\varepsilon}_{\mathbf{ij}} + \lambda \boldsymbol{\delta}_{\mathbf{ij}} \boldsymbol{\varepsilon}_{\mathbf{nm}} \tag{9}$$

where

σ_{ij} represents the symmetric stress tensor,

ε_{ij} represents the symmetric strain tensor,

δ_{ij} represents the Kroneker delta defined as:

$$\delta_{ij} = \begin{cases} 1, \text{if } i = j \\ 0, \text{if } i \neq j \end{cases} \text{ and } \varepsilon_{nm} = \sum_{i=1}^{3} \sum_{j=1}^{3} \varepsilon_{ij} \tag{10}$$

and for i=j

$$\boldsymbol{\varepsilon_{nn} = \varepsilon_{11} + \varepsilon_{22} + \varepsilon_{33}} \tag{11}$$

2.4 ***Related studies***

2.4.1 Material properties

Many researchers have conducted studies that measure the elasticity parameters of soft tissues (Azar et al., 2001; Schnabel et al., 2001). Table 2.2 provides a summary of the material properties of the breast that have been measured in previous studies.

Table 2.2 Summary of previous studies on material properties of breast

Han et al. (2012)	E=10kPa, v=0.49, density=1000 kg/m3
Krouskop et al. (1998)	E=18±7 kPa at 5% strain E=20±8 kPa at 20% strain υ=0.495
Wellman et al. (1999)	E=48±2.5 kPa at 1% strain E=17.4±8.4 kPa at 15% strain
Azar et al. (2001)	$E=b\cdot e^{m\varepsilon}$ if $\varepsilon<15.5\%$ B=4.46 kPa m=7.4 if $\varepsilon\geq 15.5\%$ b=15.1 kPa m=10 υ=0.49999
Samani et al. (2001)	$E=519.7\varepsilon^2+2.4\varepsilon+4.9$
Samani & Plewes (2004)	C_{10}=0.31 kPa C_{01}=0.3 kPa C_{20}=3.8 kPa C_{11}=2.25 kPa C_{02}=4.72 kPa
Samani et al. (2007)	E=3.25±0.9 kPa at 5% strain
Palomar et al. (2008)	C_{10}=3.0 kPa
Rajagopal et al. (2008)	C_{10}=0.08 kPa C_{10}=0.13 kPa
Lapuebla-Ferri et al. (2011)	C_{10}=0.54 kPa

2.4.1.1 Boundary conditions in FEA

A complicated biomechanical model can be built to simulate the movement of the pectoral muscles (Tang et al., 2009), or by adding a displacement boundary that takes the movement of the muscles along the chest wall into consideration (Carter et al., 2008). A study published by (Han et al., 2014) added a sliding motion to simulate the muscles.

2.4.1.2 Meshing in FEA

Mesh generation is one of the key components in FEA simulation. A quality mesh is not only required to obtain good simulation results, but also has a significant impact on the computation time and efficient usage of computational resources. A mesh is a partition of a geometric region into a set of non-overlapping sub-regions. Each sub-region is called an element and characterized by its points (also called vertices or nodes), edges and faces. Usually these elements are tetrahedrons or hexahedrons for 3D volume meshing. These element types and their attributes are presented in Figure 2.3.

The automatic generation of a tetrahedral mesh that is patient-specific was proposed by (Mohamed & Davatzikos, 2004). The elements were built from multiple-label segmented medical images. A mesh refinement method based on quality guaranteed tetrahedral elements was proposed and a post-processing method to optimize the model via changes in the mesh topology was applied after the modelling process. Nevertheless, this method cannot ensure that the final mesh edges will lie on the surface features. On the other hand, (Sullivan et al., 1997) proposed a method to move mesh nodes to single point features but it is not easy to select such features automatically. However, the accuracy of this approach is lacking to obtain accurate FE simulations.

Theoretically, hexahedral meshed models have greater accuracy than tetrahedral meshed models (Ramos & Simoes, 2006). In current practices, most commercial software packages cannot automatically generate hexahedral meshes from a complex geometry. Some researchers have therefore developed methods that use image voxels as the eight nodes of the hexahedral elements to directly convert images. However, this leads to less accurate results, especially on the surface of the model (Guldberg et al., 1998).

A voxel-based hexahedral meshing method was proposed by (Keyak et al., 1993) for medical imaging applications, which is a selective way to generate hexahedral meshes from segmented medical image sets. Voxel hexahedral meshes can be directly generated from segmented images because they are made of solid discrete voxels. Such voxels in the range of interest (ROI) in pre-segmented images will form the basis of the mesh, and then a series of regular hexahedral elements can be generated without the help of surface contours. This meshing method is robust and simple and allows for the automatic construction of hexahedral meshes from medical images. However, the surface of the model generated by using this method is not very smooth, and numerical problems may be caused by the serrated inner and outer surfaces. A study showed that an unsmooth geometry may lack elements in the region with sharp geometrical discontinuities, thus leading to the errors in modelling (Marks & Gardner, 1993). Camacho et al. reported another surface smoothing algorithm, which is very simple, and the model generates fewer errors at the surface of the model (Camacho et al., 1997). Viceconti et al. indicated that a large number of degrees of freedom needed for voxel meshing will result in less accuracy (Viceconti et al., 1998). Müller & Rüegsegger further proposed a voxel-based FEM in which the marching cubes algorithm in (Lorensen & Cline, 1987) was used, and linear tetrahedrons were used with the method to create meshes with smooth surfaces (Müller & Rüegsegger, 1995).

Generally, meshes with hexahedral elements are superior to those with tetrahedral elements in terms of convergence, stability of the solution in nonlinear systems and accuracy.

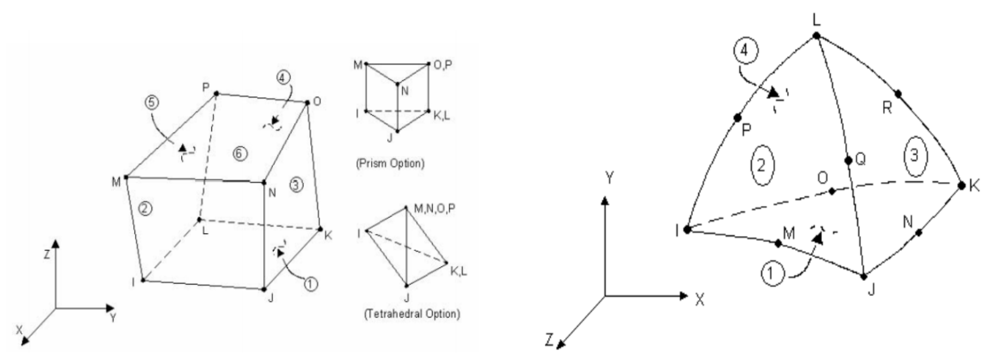

Figure 2.3. Hexahedral and tetrahedral meshes.

2.4.2 *Previous models of breasts*

As mentioned earlier, there are many types of breast imaging modalities, including x-ray mammography, MRI and ultrasound imaging, which are routine imaging modalities in clinical settings. Digital breast tomosynthesis (DBT) and PET have also recently become more available for imaging breasts. However, in each of these modalities, the positioning of the patient is different. In mammography and DBT, the breast is compressed. In MRI, the patient is in the prone position, and with PET scanning, in the supine position for an entire body scan. In ultrasound acquisition, the patient lies on a bed with her body rotated to the scanning side. The use of the ultrasound probe will compress the breast.

In response, biomechnical modeling has been used to simulate and predict the movement of breasts, which can be used in surgical and radiotherapy planning, image guided interventions and multi-modality cancer diagnosis, staging and therapy.

2.4.2.1 Compression model

Zhang et al. developed a breast compression model from MR images to simulate x-rays for a compressed situation. The model of the breast was built from 2D morphology extracted from the breast contours, and an adaptive meshing method was used to balance computation time and accuracy. Both the x-ray and MR images were from the same subject to reduce calibration errors. A model that enables the simulation of large deformations in the breast was subsequently established. A tetrahedral mesh was used, and the model was built based on the contours of the breast (Zhang et al., 2007).

Hopp et al. developed a breast image registration method by using biomechanical FEM models and intensity-based optimization. MR images were compressed to simulate x-ray mammograms. The stiffness of the glandular tissue was modeled 7.5 times higher than that of fatty tissue. The Poisson's ratio was set as 0.3. Since mechanical properties do not play an important role in compression simulation, the optimization process focused on the rotation parameter. The target registration error after intensity-based rotation optimization is 11.0±8.5 mm (Hopp et al., 2013).

Samani et al. proposed a FEM to predict breast-tissue deformations based on biomechanical principles (Samani et al., 2001). They qualitatively carried out FEM simulations of the breast by using two different approaches. First, they used a linear elastic-tissue model to simulate a 50% deformation. Then, they simulated an 8 mm compression of the breast by using a nonlinear tissue model based on the measurements of the stress–strain relationships in breast tissue made by (Wellman et al., 2001).

2.4.2.2 Gravity induced model

A study (Carter et al., 2008) modelled breast deformation in the supine and prone positions with dynamic contrast-enhanced magnetic resonance imaging (DCE-MRI). There were three steps involved in this study. First, the breast was deformed under gravity loading by using FEA. Secondly, the surface of the deformed model and prone MR image were aligned by using an iteration process. Finally, after predicting the deformation, the images were then registered with an intensity-based registration algorithm. This is also a hybrid registration framework. The results showed a mean registration error between 5 mm and 10 mm. However, this model did not consider the specifics of each patient and the breast surface was forced to match the real surface.

Krol et al. developed a PET/MRI registration model with landmarks distributed on the breast skin during scanning. However, the model was built based on the surface of the breast without taking into consideration the variance of the mechanical properties. The model was then refined based on the landmarks that were placed on the breast (Krol et al., 2006).

Eiben established a breast image registration framework for the prone-to-supine positions (Eiben et al., 2016). Both the prone and supine loaded breasts were unloaded, and then compared to updated material properties. For the loading environment, image force was also considered except for gravity. They used image force to drive the images towards the direction that registration requires. They also carried out a material optimization procedure to optimize the material parameters of the breast tissue. However, image force will reduce the reliability of optimized material properties.

Han et al. developed a patient-specific biomechanical model to predict large breast deformations (Han et al., 2014). Based on image similarity between FE-predicted and experimentally acquired MR images, they also carried out an optimization procedure for the material parameters. The parameters optimized were the Young's modulus, Poisson's ratio and the strength of fiber reinforcement. However, this simultaneous optimization is time consuming, because image similarity has to be calculated for each iteration process. The dataset was also limited, which in this case, consisted of only five cases.

A simulation model for the supine to prone positions was proposed by Palomar (Del Palomar et al., 2008). Three-dimensional scanned images were compared, and the model was found to reasonably simulate breast response to gravity force. Landmarks were manually placed on the breast for better evaluation. However, this procedure cannot be applied in clinical settings. As well, only two patients were recruited for their study, and the same elastic parameters were assigned to both patients. However, elastic parameters should be individual-specific.

Azar et al. simulated breast deformation for applications in MRI-guided biopsies (Azar et al., 2001). The geometry of the model was constructed from MR data, and mechanical properties were assigned by using a nonlinear material model defined by experiments. However, the large mesh created instability in the analysis.

2.4.2.3 Limitations

1. In a number of studies, the major limitations are that the mechanical properties are treated as a constant value for all of the models. Neglecting the heterogeneity of mechanical properties can lead to a reduction in the specificities of the breast model that is established.
2. The reference state has not been identified in most of the discussed studies, or gravity is applied twice (Carter et al., 2008; Palomar et al., 2008). Only the importance of the unloaded reference state for biomechanics was addressed by (Rajagopal et al., 2006). Therefore, in this study, a stress releasing method which is commonly found in civil engineering is used to calculate the unloaded state of the breast.
3. A validated quantitative evaluative method has not been provided in previous studies. Usually, the accuracy of deformed models is validated by using

manually defined landmarks; however, the placement of landmarks is very subjective. In this study, the images collected all have a lesion in their MR image, and therefore the landmarks do not need to be manually defined. Various quantitative parameters that can be used as the standard have been identified, except for the registration error.

2.5 ***Research questions and study objectives***

It is obvious that early diagnosis of breast cancer is essential and can significantly improve the chances of survival. Related studies have been mostly conducted in western contexts, and few have focused on the Chinese context or both western and eastern contexts. However, the breast shape, structure and properties are somewhat different among different racial groups. A model that applies to the general public will not suffice.

In the modelling processes in previous studies, both PET and MR images undergo various binary and open algorithmic processing to extract the contours of the breast. The model obtained from these contours is not patient specific. In fact, some features of the patients have been lost, and simplification can lead to misregistration in the future. The surface of the breast models is not very smooth and refinement of the surface requires time. Unsmooth surfaces will affect the FEA, thus leading to registration inaccuracies.

A general but patient-specific method with high efficiency is therefore necessary as a better solution. This study therefore aims to achieve this by addressing the following questions:

1. Will this biomechanical model make good predictions of breast deformation induced by gravity?
2. Will this patient-specific registration method improve the registration quality of breasts in clinical applications?

The specific research objectives are listed below:

1) to develop a biomechanical model that can simulate tissue deformation in the breasts, which can improve the accuracy of image registration;

2) to enhance the visualization of medical imaging, in particular, PET in combination with MRI for better diagnoses, which will improve the accuracy of breast cancer diagnosis for patients in clinical practices, and

3) to develop a biomechanical model that can non-invasively determine the mechanical properties of breast tissue.

2.6 ***Chapter summary***

In this chapter, a review of the previous studies that have used FEA to model the breast has been provided and their results evaluated. CAD and the basics of the finite elasticity theory have been outlined. The breast anatomy which is very important for building a biomechanical model of the breast has also been described. Both the advantages and disadvantages of currently available imaging modalities are discussed. Finally, the research objectives and questions have been discussed.

3 Building biomechanical model of the breast

3.1 *Image collection*

In total of 28 pairs of PET/CT images and MR images were collected from hospitals. Eight of them were from the Hong Kong Sanatorium Hospital (Siemens Biograph 40 and Siemens Trio TIM) and 20 pairs were collected from the Duke University Health System in USA (GE Discovery STE and Siemens Avanto). All the images have receive ethic approval from the Hong Kong Polytechnic University Ethic Committee.

The patient information is shown in Table 3.1.

Table 3.1 Patient information

Case No.	Lesion size (mm)	Volume (ml)	Density	Weight (kg)
US Case				
D1	22.7	687	0.17	51.7
D2	23	1584	0.10	77.1
D3	24.4	408	0.38	58
D4	24.8	601	0.20	52.6
D5	46.5	2476	0.10	99.7
D6	36.2	742	0.16	74.8
D7	4.7	493	0.17	58
D8	14.5	597	0.25	56.7
D9	18.1	924	0.49	74.8
D10	66.6	1948	0.12	115.6
D11	64.9	1442	0.26	73
D12	11.7	918	0.14	77.6
D13	15.7	1078	0.12	66
D14	48.9	566	0.07	62.6
D15	19	1055	0.08	95.3
D16	38.2	3779	0.03	113.4
D17	12.8	597	0.24	54
D18	41	1728	0.03	113
D19	28	3252	0.17	112
D20	19	2851	0.10	85
HK Case				
H1	37	386	0.46	70
H2	14.8	1072	0.17	68
H3	23.8	852	0.13	65
H4	18.3	776	0.27	60
H5	NA	766	0.13	33
H6	30.1	582	0.13	60
H7	22.5	670	0.57	75
H8	61.3	757	0.37	65

3.2 *Effects of skin on modelling*

3.2.1 Introduction

As stated in Chapter 2, the breast contains adipose tissue, fibro-glandular, skin, and Cooper's ligaments. In the following, the effects of modeling the skin of the breasts are investigated.

A Study (Li et al., 2012) indicated in their study that skin comprises three layers: the epidermis, dermis and fatty subcutaneous layers. The deepest layer is the subcutaneous fat layer, which has the least stiffness (around 34 kPa) compared with the other layers of skin. The thickness is over 1.2 mm (Li et al., 2012). For the dermis layer, the Young's modulus is around 88 to 300 kPa (Gennisson et al., 2004; L'Etang & Huang, 2006; Liang & Boppart, 2010) and its thickness is around 1 mm. Finally, the top layer is the epidermis layer, which has the highest Young's modulus of approximately 1 MPa, with a thickness of 0.1 mm (Xu et al., 2008).

3.2.2 Method

Since it is difficult to completely segment skin from CT images, skin was modeled by adding a layer of shell elements that was 1 mm in thickness to the anterior face of the model. This layer of elements was tightly coupled with the elements of breast tissue. Skin was assigned a density of 1000 kg/m^3 (ICRP, 2009), and Poisson's ratio of 0.49. It obeys a Neo-Hookean constitutive relationship.

The deformation was simulated on a half sphere phantom. Nine FEAs were carried out with a varying Young's modulus of the skin from 40kPa to 1000kPa, and an additional study with no skin. At the same time, the mechanical properties of the other parts of the breast were not varied. The node displacements of the nipple are listed in Table 3.2.

3.2.3 Results

Nine sets of Young's moduli of the skin were applied to perform the analysis. The differences ranged from 3.3%-12.2%, and the maximum difference was with a Young's modulus of 40 kPa.

Table 3.2 Nipple displacement with different Young's moduli of skin

Young's modulus (kPa)	40	100	300	600	700	800	900	1000	No skin
Nipple displacement(mm)	13.8	13.7	13.4	13.0	12.9	12.9	12.8	12.7	12.3

3.2.4 Conclusion

The node displacement changes either with the addition of a layer of skin or increased stiffness of the skin. The result indicates that by adding a layer of shell mesh as the skin to model breast deformations in the supine to prone positions will increase nipple displacement. A study (Gefen & Dilmoney, 2007) indicated that the range of the Young's modulus of the skin is between 200-3000 kPa. In this study, I chose to use a Young's modulus of 1000 kPa of the skin.

3.3 *Computing reference state*

To compute the reference state, the following methods can be used. The first method is to reverse the direction of gravity. In linear elasticity domains, the reference state can be computed by reversing the direction of gravity. However, this does not apply to breast tissue since it is non-linear heterogeneous soft tissue.

The second method is to estimate the initial stress. When a patient is in a supine or prone position, her breasts experience internal stress caused by gravity. Therefore, computing the internal stress of each node can be carried out. After adding these stresses to the breast model, the exact state of the breast is established.

The third method is an iteration process. A study (Rajagopal et al., 2006) used this method to identify the reference state of the breast. A load was added to the deformed breast to predict deformation, and then this breast model was compared with a real model, and the iteration process continued until matching.

The use of an iteration process to identify the reference state means a large amount of computation work. Therefore, I will use the second method, which is estimating the initial stress, to build a reference state for the breast. A general material property of 1000 kPa was assigned as the Young's modulus and 0.45 as the Poisson's ratio.

3.4 *Mesh sensitivity study*

3.4.1 Introduction

Mesh sensitivity can represent the quality of a finite element mesh. Technically, despite other inputs, high quality meshes produce results with an acceptable level of accuracy. Mesh density can control the accuracy of the model, and a model with a high density mesh has high accuracy. However, if the mesh density is too large, the computation time will greatly increase. Therefore, the mesh density can be measured to represent the mesh sensitivity.

A way to evaluate the quality of meshes is to compare the results with test data or theoretical values. Unfortunately, both are not available for this research work. So, other means of evaluating mesh quality are needed. These could include mesh refinement and interpretations of results discontinuities. The most fundamental and accurate method for evaluating mesh quality is to refine the mesh until a critical result is obtained (Hale, 2014). As the maximum stress does not significantly change with each refinement, it is used as the standard.

3.4.2 Method

To evaluate the mesh quality, the mesh is refined until a critical result is acquired. In this study, as shown in Figure 3.1, the initial model is (a) and the deformed model is (b), different mesh density was assigned with the initial model to conduct analysis. According to the color bar of stress distribution (d), the maximum stress appears to be the edge of the bottom plate (c). The convergence of the results is the maximum stress. The density of the mesh is increased until the maximum stress converges. The density of mesh increased from 8 elements to 360 elements per unit area. The

Maximum von Mises stress at the junction between the bottom and the circular surface is calculated under each mesh density.

3.4.3 Results

To identify the suitable mesh size for this study, I measured the mesh sensitivity by reducing the mesh size until the changes in the maximum von Mises stress at the junction between the bottom and circular surface is the smallest. A series of mesh densities were used to generate meshes. After the FEA was carried out, the maximum von Mises stress of each density is plotted in Figure 3.2. The results show that a mesh density that contains around 60 elements per unit area can provide the most stable model.

3.4.4 Conclusion

In this study, an increase from 61 elements to 110 elements per unit area yields only a 7.09% increase in stress, which is the smallest change. Further increases in the mesh density does not significantly increase the maximum von Mises stress. Therefore, the mesh density chosen is approximately 60 elements per unit area.

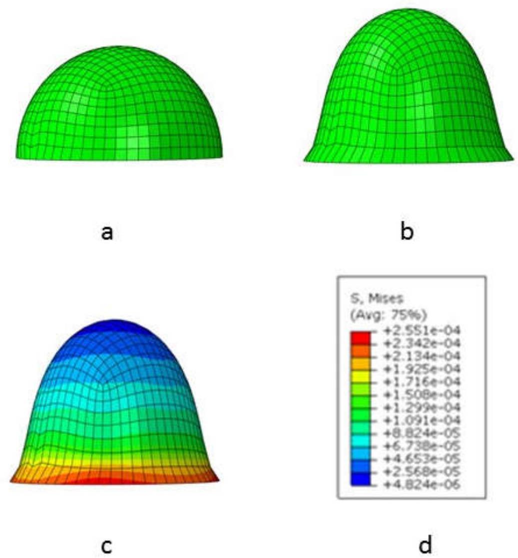

Figure 3.1 Hemisphere phantom in (a) unload state, and (b) deformed state, and (c) stress distribution and (d) color bar of stress.

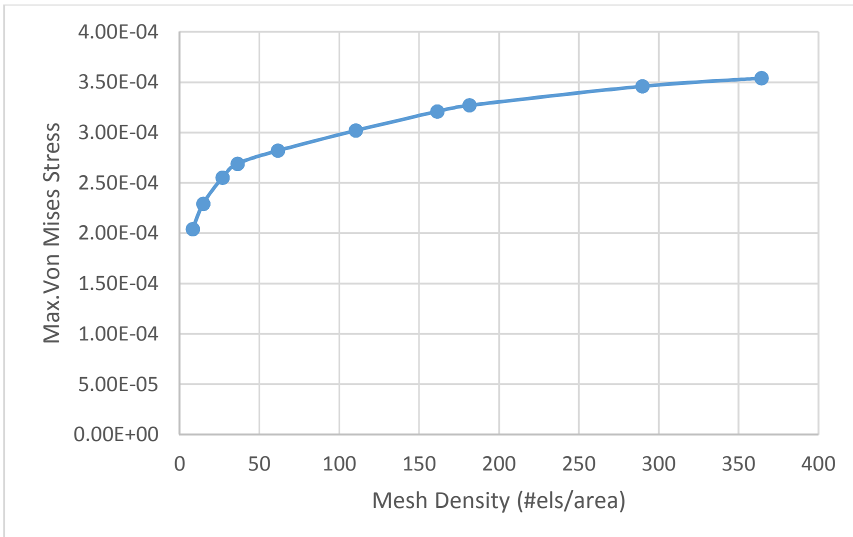

Figure 3.2 Maximum von Mises stress for different mesh densities

3.5 *Element shape*

3.5.1 Introduction

To build a biomechanical model for FEA, it is important to choose a mesh that is more accurate and efficient to carry out the analysis. There are two kinds of meshes that are commonly used to build a finite element model, which is tetrahedron and hexahedral meshes.

In this section, a phantom is created to determine whether a hexahedral or tetrahedral mesh should be used to simulate the deformation of breasts from the supine to prone positions.

3.5.2 Method

The phantom is a hemisphere model. The density of the phantom was assigned as 1000 kg/m^3. The radius of the half sphere was 50 mm. The material of the phantom has a Neo-Hookean strain energy function. The material parameters were assigned a Young's modulus value of 1000 kPa, and a Poisson's ratio of 0.45. A gravity of 9.81 m/s^2 was applied perpendicular to the bottom face of the half sphere phantom. The direction was from the flat bottom face to the hemisphere. This model is regarded as the reference state. Both the hexahedral (C3D8R) and tetrahedral (C3D10) meshes were created respectively. The meshes were generated by obeying the following rules.

1. The meshes have the same number of nodes. The hexahedral mesh has 26,420 nodes and 24,300 elements. The tetrahedral mesh has 25,139 nodes and 17,272 elements.

2. The meshes have the same number of elements. The hexahedral mesh has 26,420 nodes and 24,300 elements, while the tetrahedral mesh has 35,212 nodes and 24,427 elements.

There were no bad elements in both mesh models.

3.5.3 Results

The deformed and undeformed meshes are shown in Figure 3.4. According to the deformation of the hemisphere phantom, mesh type does not significantly affect deformation. Therefore, the mesh is chosen based on computation time. The calculation time is shown in Table 3.3. The tetrahedral mesh which has the same number of elements as the hexahedral mesh requires the longest computation time. When the number of nodes is the same, the hexahedral mesh requires the shortest computation time.

3.5.4 Conclusion

The hexahedral mesh requires less time to solve a problem, even with the same number of nodes or elements as the tetrahedral mesh. The hexahedral mesh also provides a structured mesh, with all the nodes distributed onto a grid.

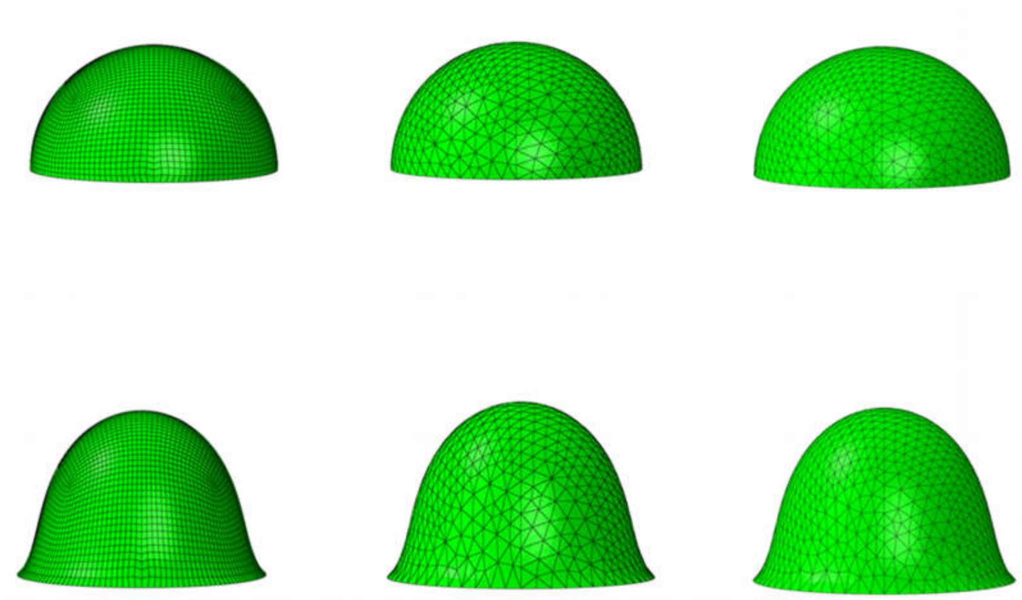

(a) **(b)** **(c)**

Figure 3.3 Hemisphere phantom in reference state (upper) and deformed state (lower) for (a) hexahedral mesh with 24,300 elements, (b) tetrahedral mesh with 17,272 elements and (c) tetrahedral mesh with 24,427 elements

Table 3.3 Computation time required for hexahedral and tetrahedral meshes due to gravity-induced deformation.

Element shape	Number of elements	Number of nodes	Calculation time (s)
Hexahedral	24300	26420	59
Tetrahedral	17272	25139	62
Tetrahedral	24427	35212	103

3.6 ***Compressibility***

3.6.1 Introduction

The Poisson's ratio reflects how much the volume of a material changes during deformation. Since biological tissue contains incompressible fluid (water), it is commonly described as 'incompressible' (Fung & Tong, 2001). However, when patients undergo PET/CT scanning in the supine position and MR scanning in the prone position, the length of time elapsed between the prone and supine imaging procedures means that the volume of the breast might have changed due to the changes in the fluid content.

3.6.2 Method

To identify the Poisson's ratio of breast soft tissue, the volume changes of the breast in the supine to prone positions were examined. The MR images were cropped as a box in accordance with the CT image. The length of the box in the y direction was determined by the distance between the bottom lines and chest wall. This distance should be the same as that in the CT image. This is to ensure that the breast volume in the MR and CT scans is not affected by definition of the boundaries. The breast volume in both the MR and CT images was calculated for three pairs of images.

Three pairs of CT images and MR images (D3, D4 and D6) of the 20 pairs of image cases collected from the US were used to calculate the volume change.

3.6.3 Results

The breast volume in the prone and supine images and the calculated changes in the volume for three subjects (D3, D4 and D6) of the 20 cases form the US are provided in Table 3.4. The percentage of the volume change in the prone to supine positions ranges from 2% to 7%, which is very small.

3.6.4 Conclusion

The change in breast volume measured in this study is small. The results support the incompressible nature of breast tissue. Therefore, the Poisson's ratio is assigned a value of 0.45.

Table 3.4 Breast volume change in prone to supine position.

Subject	Volume in prone (ml)	Volume in supine (ml)	Volume change from supine to
D3	420	408	3%
D4	614	601	2%
D6	794	742	7%

3.7 *Image Preparation and Segmentation*

3.7.1 Image preparation

The image resolution of MR images is 1.3 pixels per mm, the resolution of PET image is around 0.26 pixels per mm in this study. Hence, this large difference between the PET and MR images can reduce the accuracy of image registration later. Both CT and PET images were interpolated to a resolution of 1 pixel per mm, and the MR images were also interpolated to a resolution of 1 pixels per mm. When the resolution is the same, further processing becomes easier.

3.7.2 Segmentation

As mentioned in Chapter 2, the breast mainly consists of adipose and fibro-glandular tissues. Adipose tissue is apparently softer than fibro-glandular tissue. A general model that treats the entire breast as a homogenous entity that contains only one kind of material is therefore not realistic. Therefore, the CT image was segmented before building the model.

Three segmentation methods have been considered in this research work: fuzzy-c means, Markov random field and histogram threshold segmentations. Image segmentation is one of the most challenging tasks in the field of image processing. It is basically the process of assigning a label to every pixel in an image, and all pixels that share the same label have the same visual characteristics.

3.7.2.1 Histogram threshold segmentation

In the modeling of intensity, it is assumed that there are three classes of glandular, fat and background tissues respectively. However the modeling of intensity alone can only give accurate results when the intensities for different tissues are well separated. The problem with adipose and glandular tissues is that there are many voxels that represent these two types of tissues.

3.7.2.2 Fuzzy-c means

Fuzzy c-means (FCM) is a data clustering technique, in which datasets are grouped into a number of clusters. This method was developed by (Dunn, 1973) and amended by (Bezdek, 2013). FCM is a widely used unsupervised segmentation technique, and therefore can make good predictions and classifications based on the observation of a given image.

3.7.2.3 Markov Random Field

In real images, regions are often homogenous; neighboring pixels usually have similar properties (intensity, color and texture). Markov Random Field (MRF) is a probabilistic model which captures such contextual constraints(Kato & Pong, 2006). MRF theory provides a convenient and consistent way of modeling context-dependent entitles such as image pixels and correlated features (Li, 2009).

Segmentation that uses Markov random fields is also unsupervised segmentation, which extracts features from the inputted image, and also takes neighboring pixels into consideration. However, in a breast image, pixels on the edge of a tissue, for example, the adipose tissue may be erroneously misclassified as, for instance, the glandular tissue.

To better identify the breast tissue, Markov random field regularization is an appropriate choice due to the anatomy of the fibro-glandular tissues. Since the breast ducts are connected in a tree-like structure inside the breast, the voxels that represent the glandular tissue are more likely to be connected to other voxels of glandular tissue, rather than isolated inside the fatty tissue.

Typically, a breast with a lesion should be subdivided into at least three parts: fatty tissue, tumor and fibro-glandular tissue. As it is difficult to identify the intensities of tumors in CT imaging, the breast is only segmented into two parts in this study, which are fatty and fibro-glandular tissues. However, as shown in Figure 3.4, the FCM segmented image has some black holes in the fibro-glandular tissue, but the whole fibro-glandular tissue will be used to build a solid fibro-glandular model. The computation times of a single slice with the use of these two methods are listed in Table 3.5. It can be seen that FCM requires less computation time. In some case, the image is over segmented, the pixels out of the boundary is also considered as adipose or fibro-glandular tissue.

Therefore, based on the computation time and segmentation performance, FCM is applied in this research work to carry out fast segmentation.

Table 3.5 Computation time for FCM and FRM

	D14	**D11**	**D6**
FCM	0.39s	0.64s	0.71s
MRF	6.77s	8.03s	7.56s

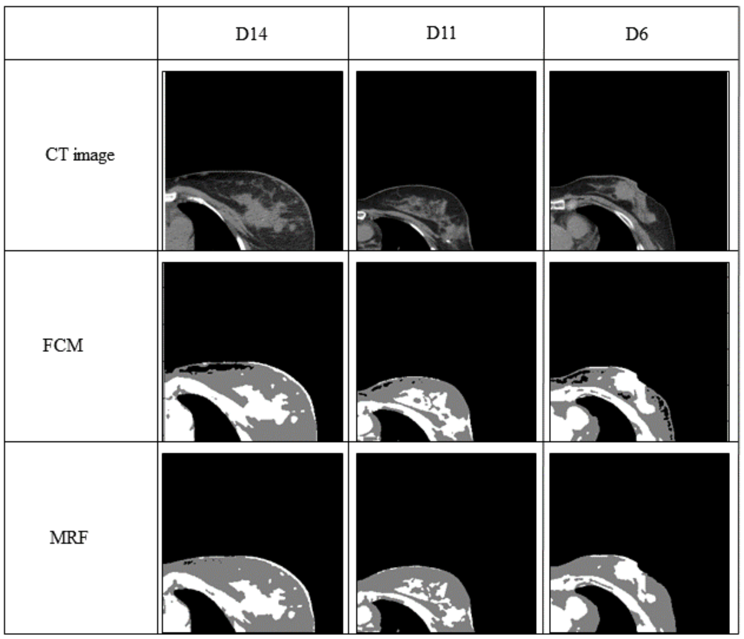

Figure 3.4 Segmentation results of FCM and FRM for three cases of the 20 US cases.

3.8 *Chapter summary*

This chapter has described the aspects considered when constructing a finite element model of the breast.

To ensure the quality of breast modeling, I recorded the computation time required by both the hexahedral and tetrahedral meshes. When the number of nodes is the same, the hexahedral mesh requires less computation time. When the number of elements is the same, the hexahedral mesh again requires less computation time. Therefore, this result proves that the hexahedral mesh is more efficient in processing the analysis.

After deciding on the element shape, the mesh size is also considered in this chapter. Technically, a smaller mesh size can result in higher accuracy compared to a larger mesh size. However, a dense mesh also means more computation time. The results show that a mesh density that contains around 60 elements per unit area can provide the most stable model.

Another important parameter that was determined in this chapter is the Poisson's ratio. The compressibility of the breast model is calculated by the breast volume in the prone to supine positions. There are minimal changes in the volume. Therefore, a Poisson's ratio is assigned a value of 0.45.

Finally, to build a patient-specific breast model, the breast image is segmented into the adipose and fibro-glandular tissues. The segmentation methods have been discussed and summarized. FCM segmentation is applied in this study because it has the ability to perform a fast and highly accurate segmentation.

4 Image registration for patient-specific biomechanical model of the breast

4.1 *Introduction*

Breast cancer is the second most prevalent type of death causing cancer worldwide (40,450 (breast cases) out of 281,400 (all cancers)) (American Cancer Society, 2016a). The diagnosis of breast cancer will have serious repercussions for a woman as her quality of life will be negatively affected. There are 246,660 anticipated new cases of breast cancer in the United States (American Cancer Society, 2016a). However, better treatment approaches can reduce mortality rates and lead to better quality of life. Breasts are composed of soft tissues, which deform very easily when the body is in different positions. The simulation of large deformations of the breasts is a crucial element in many medical applications, such as image registration, image guided surgery, cancer diagnosis and surgical planning (Han et al., 2012). Building a mechanical model will greatly assist in these medical applications.

FEA (Zienkiewicz et al., 1977) is widely used in engineering disciplines, such as civil and mechanical engineering. It is a numerical means for finding solutions to complicated problems. FEA is also widely used in medical research. It has a dominant role in biomechanics, a means by which researchers can use to analyze stress and strain of bone under particular loading environments.

In this study, I have used FEA to establish a registration model of breast images, especially for MR and PET/CT images of the breast. CT image was used to form a patient-specific model based on the anatomical structure. As there is a high level of correlation with the material properties, a registration model by using FEA thus becomes more patient-specific.

The DIR technique has been widely applied for radiotherapy planning (Foskey et al., 2005) and image guided therapy (Sarrut, 2006). The modeling of the deformation of breast tissue have been studied by many researchers (Azar et al., 2000; Gamage et al., 2012; Gamage et al., 2011; Kuhlmann et al., 2013; Palomar et al., 2008; Pathmanathan et al., 2008; Rajagopal, 2007; Samani et al., 2001). Biomechanical modeling is used to simulate the deformation of breasts under gravity loading (Palomar et al., 2008; Rajagopal, 2007), compression in the mammography process (Pathmanathan et al., 2004; Pathmanathan et al., 2008), and in biopsy processes (Azar et al., 2000). However, none of these studies has considered material properties to be a patient-dependent parameter. Breast mainly consist of soft tissues; the adipose and fibro-glandular tissues. The latter is more stiffer than fat tissue. A breast with more adipose tissue is therefore softer, and the deformation will be greater. This is a challenging problem for researchers. Also, aside from the density differences of the adipose and fibro-glandular tissues, the distribution of fibro-glandular tissues, Cooper's ligaments and skin also affect the amount of deformation. This registration model based on an FEA will therefore take material properties into consideration.

A study by Lee et al. showed that biomechanical modeling alone is not sufficient for accurately predicting deformation (Lee et al., 2010). A registration method that combines biomechanical modeling with a non-rigid transformation registration method will provide better results. In this study, a registration process that combines FEA and affine transformation to register PET images in the supine position and MR images in the prone position is proposed.

Different imaging modalities have been used for detecting breast cancer, such as CT, MRI, x-ray mammography and PET. PET is a molecular imaging modality, which can recognize breast cancer at the molecular level to provide an early diagnosis and thus treatment. The accuracy of PET diagnoses is 8-43% higher than those of CT and x-ray mammography (Moskowitz, 1995). However, PET images have low spatial resolution and show limited anatomical information which make it difficult to locate the potential lesion(s) (Smith et al., 2004). To enhance the image quality of PET, a registration process needs to be developed which combines PET imaging with another imaging modality such as MRI which shows anatomical structural information (Antoch & Bockisch, 2009). Although patients may not be able to undergo PET and MRI scanning at the same time, the registration of PET and MRI is still necessary. Due to the differences in the resolution of PET and MRI and image formation processes, the intensity relationship between PET and MR images cannot be defined. The registration of MR and PET images based on similarity measures provides unsatisfactory results (Unlu et al., 2010). Here, an FEA-based registration model for PET and MR images is proposed, which takes patient-specific features into consideration.

4.2 ***Method***

The large-scale deformation of breast is predicted to register the PET/CT image in supine position with MR image in prone position. The registration procedure includes three part in total as shown in Figure 4.1.

Part1: Generate an FE model from the CT image.

Part2: FEA and optimize the mechanical properties, the process of FEA is shown in Figure 4.2.

Part3: Align the FEA predicted image in prone position with the original MR image in prone position.

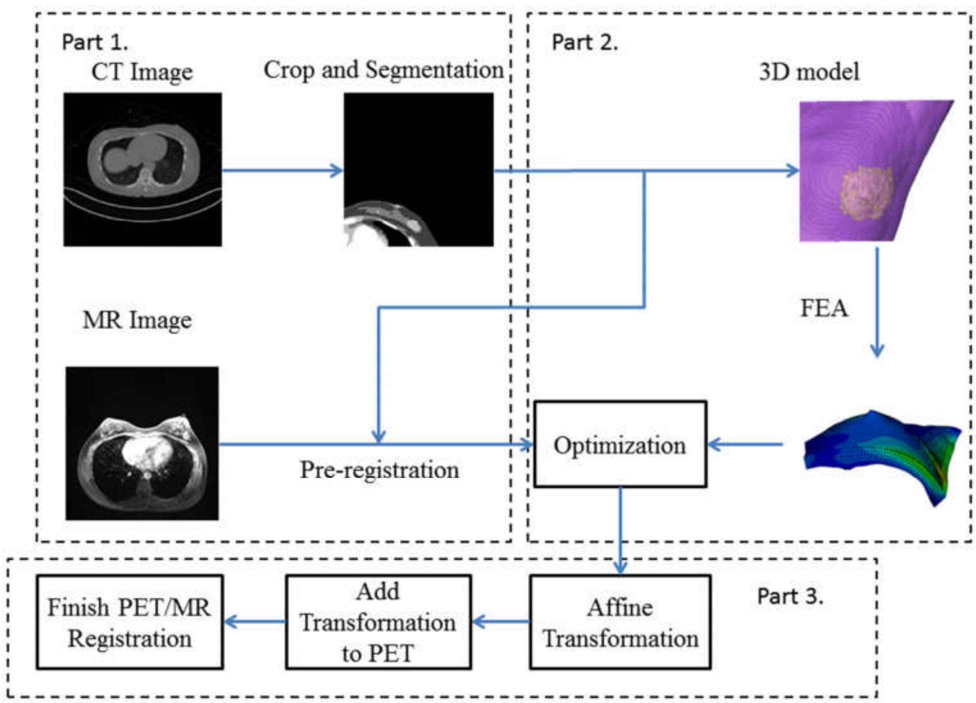

Figure 4.1 Flowchart of registration process

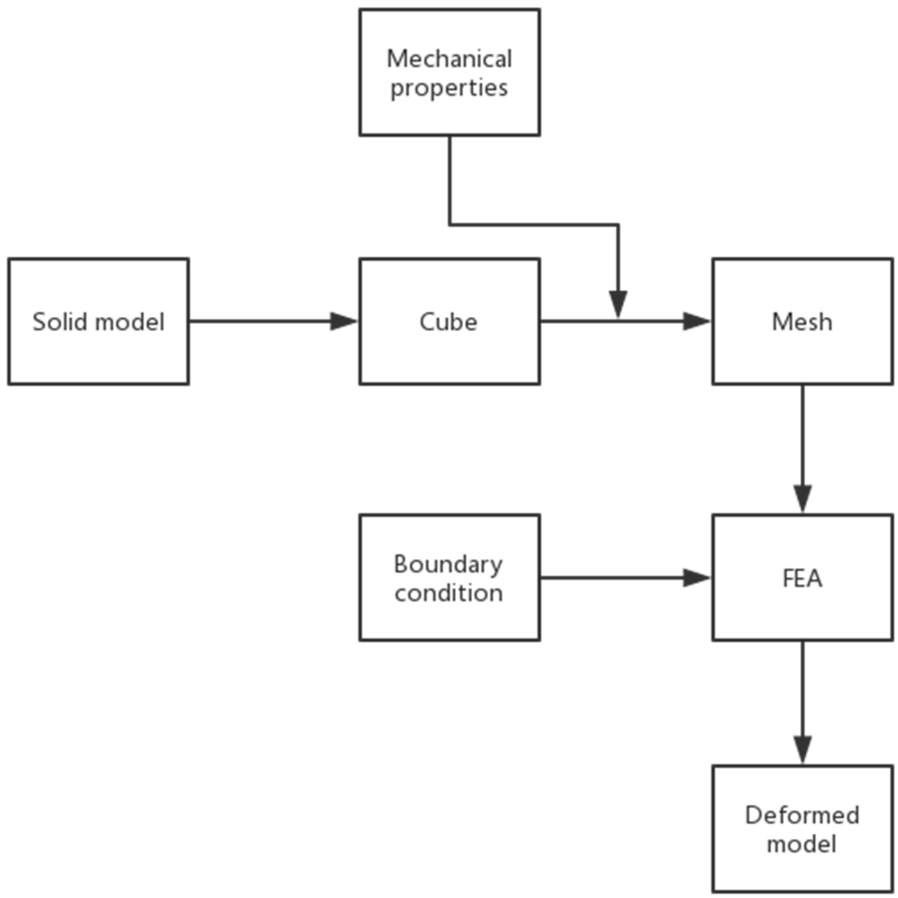

Figure 4.2 Flowchart of FEA.

4.2.1 Preprocessing

Eight PET/CT and MR images were collected from Hong Kong Sanatorium Hospital (Siemens Biograph 40 and Siemens Trio TIM). In each case, the CT volume was cropped, and the left or right breast was selected based on a lesion on the MR image. Breast images between the second and the seventh ribs were used to build the breast model. The Cooper's ligaments were neglected because they were not visible in the images. The CT breast image was segmented into the adipose and fibro-glandular tissues automatically by using an FCM algorithm (Bezdek et al., 1984). The chest wall and muscle were manually segmented from the breast, and then 3D models of the fatty and fibro-glandular tissues (Figure 4.3) were built based on these segmented images via marching cube operation respectively (Lorensen & Cline, 1987).

Figure 4.3 Segmented breast model (fatty tissue - dark gray color, fibro-glandular tissue - light gray color).

4.2.2 Patient-specific model

As shown in Figure 4.3, the 3D breast model is generated by merging the modeling of the fatty tissue (green color) with the fibro-glandular tissue (gray color) together. Breast skin was modeled by adding a 1 mm mesh layer on the surface of the breast model. FEM was used to simulate the physical behavior of the breast during the deformation process.

In order to improve the efficiency of operation during the FEA, the model was cut into cubes to generate finer hexahedral meshes as shown in Figure 4.4(a) and 4.4(b). The model was assigned a homogeneous isotropic material. The stiffness ratio of the fibro-glandular and fatty tissues was chosen based on published data. The Young's modulus of the fibro-glandular tissue was modeled 7.5 higher than the fatty tissue (Hopp et al., 2013). The Poisson's ratio used in this study is 0.45 because according to previous studies, breasts are considered incompressible (Azar et al., 2001; Palomar et al., 2008; Rajagopal et al., 2006; Samani et al., 2001). A neo-Hookean constitutive relationship was used to predict the nonlinear stress-strain behavior of hyperplastic materials (Bonet & Wood, 1997), and proven to be reliable in accurately representing the mechanical behavior of incompressible isotropic soft tissue (Chung, 2008; Chung et al., 2008). Physical behavior is also described by the boundary conditions, in which the surface that is connected to the chest wall is fixed in the anteroposterior direction to simulate the fixation at the chest wall (Hopp et al., 2013).

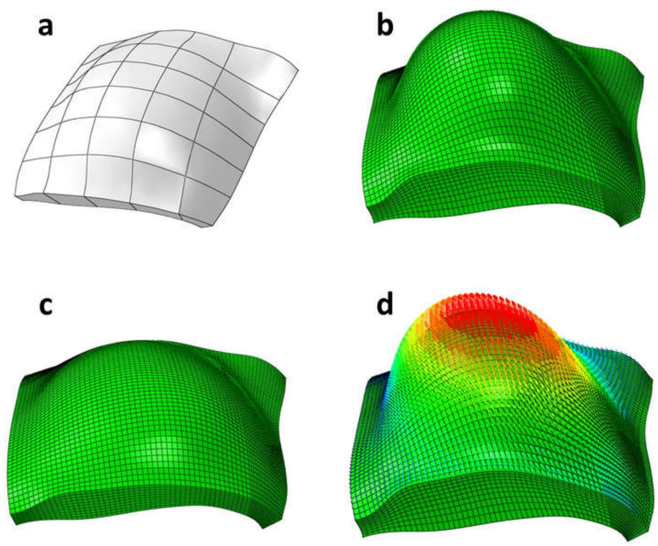

Figure 4.4 3D model of breast and breast deformation simulation. (a) generated 3D breast model and segmented into small cubes for finer mesh; (b) hexahedral meshes created based on cubes, (c) simulation of breast deformation under gravity, and (d) nodal deformation vector plotted on each node to illustrate movement of nodes during deformation.

4.2.3 *Deformation Simulation*

The deformation of the breast was predicted by using ABAQUS (Hibbett et al., 1998). Displacements equal to zero were assigned to the surface that connected with the chest wall in the X, Y, and Z directions. Gravity loading was added along the vertical direction.

All images of the breast were obtained under a gravity loading environment, regardless whether the imaging was CT, PET or MRI. Therefore, the model built from the images is a deformed model in loading conditions. Identifying the unloaded geometry of the breast is required to simulate the deformation of the breast from the supine to the prone positions. The reference state of the breast is a load-free state. Identifying the reference state allows for a more reliable prediction of deformation (Rajagopal et al., 2006). Rajagopal et al. (Rajagopal et al., 2006) developed a method to calculate the reference state of the breast by using an iteration process. In this study, the initial stress was estimated in ABAQUS, and the initial stress was released to calculate the reference state in ABAQUS.

The initial material properties of the breast for inputting are shown in Table 4.1. The deformed model after FEA is carried out is shown in Figure 4.4(c).

Table 4.1 Initial material properties of breast.

	Density (kg/m3)	Young's modulus (kPa)	Poisson ratio
Fatty	1000	250	0.45
Fibro-glandular	1200	1875	0.45

4.2.4 *Optimization and hybrid registration*

The differences in the resolution and intensities between PET/CT and MRI make it difficult to define the correspondence between PET/CT and MR images. There are no distinct landmarks except for the nipple, fibro-glandular tissues and lesion. Fibro-glandular tissue and the lesion were used as the landmarks to evaluate the registration, therefore nipple was used as a landmark to identify the correspondence between the CT and MR images. A rigid pre-registration of the MR images for the prone position and CT scans for the supine position was performed to calculate the displacement of the nipple. This displacement could be treated as the criterion of model deformation performances during optimization.

Young’s modulus has been considered as an important factor that could influence the deformation of the breast. However, the density of a material changes the overall deformability of the breast, therefore, density is also an important factor.

Analyses were conducted to calculate the weight proportion of density, Poisson's ratio, and Young’s modulus. Since these three parameters are independent variables, three rounds of studies were designed. In each round, one factor was changed ten times while the other two factors were kept constant, and nipple displacement was calculated in each round. The correlation of density, the Young's modulus, and Poisson's ratio with nipple displacement is 0.7, 0.6 and 0.1 respectively as shown in Figure 4.5. This means that the simulation of the deformation is also very sensitive to the tissue density. However, density and the Young’s modulus are both mechanical properties. A material with a higher Young’s modulus tends to have a higher density as shown in Figure 4.6 (University of Cambridge/Department of Engineering, 2002). Here, the effects of density are neglected because the density cannot be determined based on the Young's modulus. Also, lightweight material also has the tendency to have a lower Young's modulus.

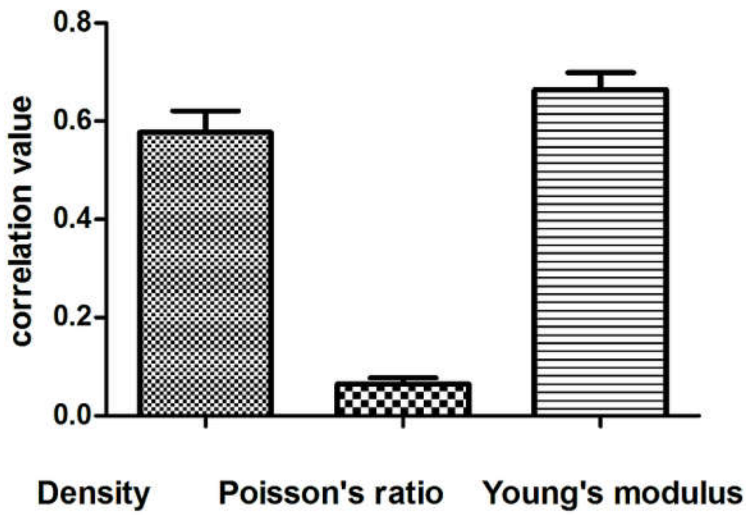

Figure 4.5 Effects of tissue density, Poisson’s ratio, and Young's modulus during breast deformation under same loading environment. Note that effects of tissue density and Young’s modulus are much higher than Poisson’s ratio.

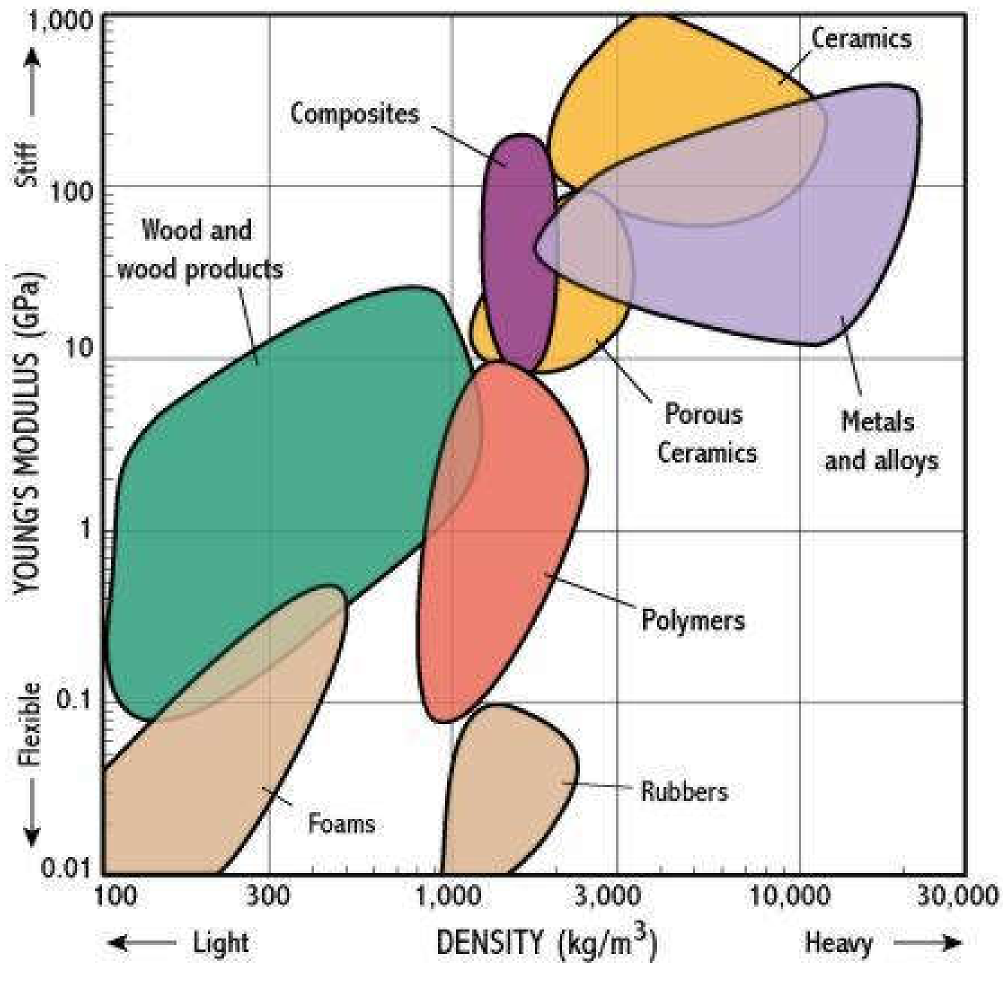

Figure 4.6 Young's modulus and density (University of Cambridge/Department of Engineering, 2002)

An optimization process was carried out after the first round of FEA simulations. Optimization was realized by using MATLAB (MATLAB2015, The MathWorks Inc., Natick, MA). The displacement vector of the nipple calculated in the pre-registration step was taken as the standard for iteration. The factor optimized was the Young's modulus of the adipose and fibro-glandular tissues. The iteration procedure is shown in Figure 4.7. The optimization process was stopped when the difference between the simulated and actual nipple displacements was within 1 mm. Equation 12 is used to determine the stopping criteria of the optimization process of the Young's modulus:

$$\text{Argmin}{-}\text{Vn subject to lb} < \text{E} < \text{ub} \tag{12}$$

where Vn represents the deformation vector of the nipple, E denotes the Young's modulus, lb is the lower bound constraint for E, and ub is the upper limit constraint for E. The boundary conditions were assigned in accordance with Equation 2:

$$0.5\text{kPa} < \text{E} < 500\text{kPa} \tag{13}$$

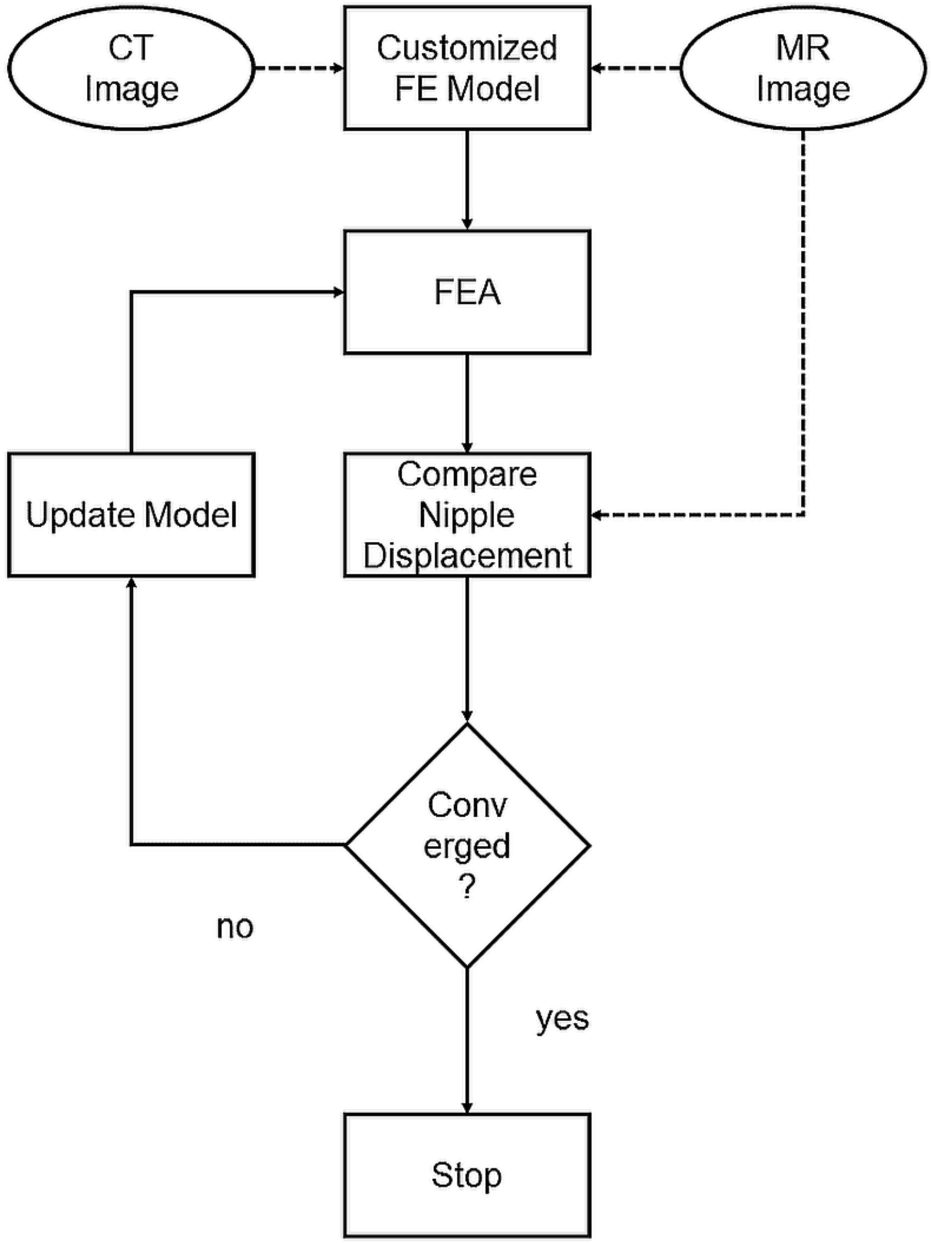

Figure 4.7 Optimization process: customized FE model built with CT images. After first round of analysis, predicted nipple displacement compared with real displacement in MR image. Model then updated by refining material properties until nipple displacements converged.

After optimization, the node coordinates of the deformation and pixel intensity values of the CT images were linearly interpolated to generate the predicted CT image in the prone position.

Affine transformation was combined with the registration of the deformities simulated by the use of FEA to create a hybrid registration, which would further improve the quality of the registration. As CT and PET share the same coordinate system, the affine transformation was conducted on the CT images and then transferred to the PET images.

Scale invariant feature transform (SIFT)-based registration can be used to register objects that are located in different regions in a robust manner. Two separate images of the same object but with different spatial information are aligned (Liu et al., 2011). This method has been used in previous studies to perform mammography and MRI registration (Zhong & Chen, 2014); (Martel et al., 2007). SIFT-based registration is therefore applied for comparing the groups of MR and PET images in this study.

4.2.5 Evaluation metrics

To evaluate the performance of the CT and PET images of the deformation, six parameters were used, namely: mutual information (MI), correlation ratio (CR), structural similarity index (SSIM), dice coefficient (DICE), target registration error (TRE) and the relative target registration error (TRE_{rel}). The landmark used to calculate the TRE and TRE_{rel} was the lesion displacement.

The DICE value is the sum of the overlapping points divided by the total number of points. It is calculated based on CR/MR and PET/MR images. DICE was calculated from area A in the MRI landmark, and defined as polygon P_{MRI} and the PET landmark defined as polygon P_{PET}:

$$D = \frac{2A(P_{MRI} \cap P_{PET})}{A(P_{MRI}) + A(P_{PET})} \tag{14}$$

The graphic centroid of the landmark in both the predicted PET and MR images was identified. The TRE is defined as the Euclidean distance between the centroid of the landmark in the MR image (C_{MR}) and PET image (C_{PET}). TRE can be used to evaluate the registration performance. It is calculated from PET/MR and CT/MR.

$$\mathrm{TRE} = ||C_{MR} - C_{PET}|| \tag{15}$$

Since the size of the landmark also affects the accuracy, TRE_{rel} is calculated per (Hopp et al., 2013), which is defined as the TRE divided by the diameter of the landmark in MRI D_{MRI}. It is calculated from PET/MR and CT/MR.

$$TRE_{rel} = \frac{TRE}{D_{MRI}} \tag{16}$$

The definition of CR, MI and SSIM, is showing below. This three metrics are calculated from CT/MR images.

$$\mathrm{CR} = \frac{\sum_m \sum_n (CT_{mn} - \overline{CT})(MR_{mn} - \overline{MR})}{\sqrt{(\sum_m \sum_n (CT_{mn} - \overline{CT})^2)(\sum_m \sum_n (MR_{mn} - \overline{MR})^2)}} \tag{17}$$

$$MI(MR;CT)=H(MR)+H(CT)-H(MR|CT) \tag{18}$$

$$\mathrm{SSIM(CT, MR)} = \frac{(2\mu_{CT}\mu_{MR+C_1})(2\sigma_{CTMR} + C_2)}{(\mu_{CT}^2 + \mu_{MR}^2 + C_1)(\sigma_{CT}^2 + \sigma_{MR}^2 + C_2)} \tag{19}$$

4.3 *Results*

Eight breast image sets were used in this study. Each set of images consists of patient CT/PET and MR images. The related information is shown in Table 4.2.

Table 4.2 Breast image basic information: volume and density of the breast image, the age of the patient, the lesion diameter, and the fibro-glandular tissue diameter.

Case no.	Volume (ml)	Age (years)	Lesion diameter (mm)	Fibro-glandular diameter (mm)	Density[a]
H1	386.131	41	37	37	0.4600
H2	1072.997	46	14.8	68	0.1700
H3	852.087	77	23.8	106	0.1300
H4	776.251	63	18.3	143	0.2700
H5	766.586	33	4.6	167	0.1300
H6	582.337	27	30.1	60	0.5700
H7	670.094	39	22.5	185	0.3600
H8	757.159	34	61.3	103	0.4600

[a] Density in this form is a volume of glandular tissue divided by volume of breast.

4.3.1 Image performance

Figure 4.8 shows how the established method predicts breast deformation from the supine to prone positions. The method used in this study successfully registers MR images in the prone position and PET/CT images in the supine position. Figure 4.9 presents the registered PET/MR images, with the lesion in the PET image colored in red. The PET and MR images were also registered by using SIFT-based registration for comparison purposes (Figure 4.10). The lesion cannot be clearly observed in the MR and PET images for S5, so the registered PET/MR image is not shown in Figure 4.9. As can be observed, the method in this study accurately predicts the location of the lesion with a TRE=4.77±2.20 mm, which is not the case for SIFT-based registration. The reason will be elaborated in the discussion section.

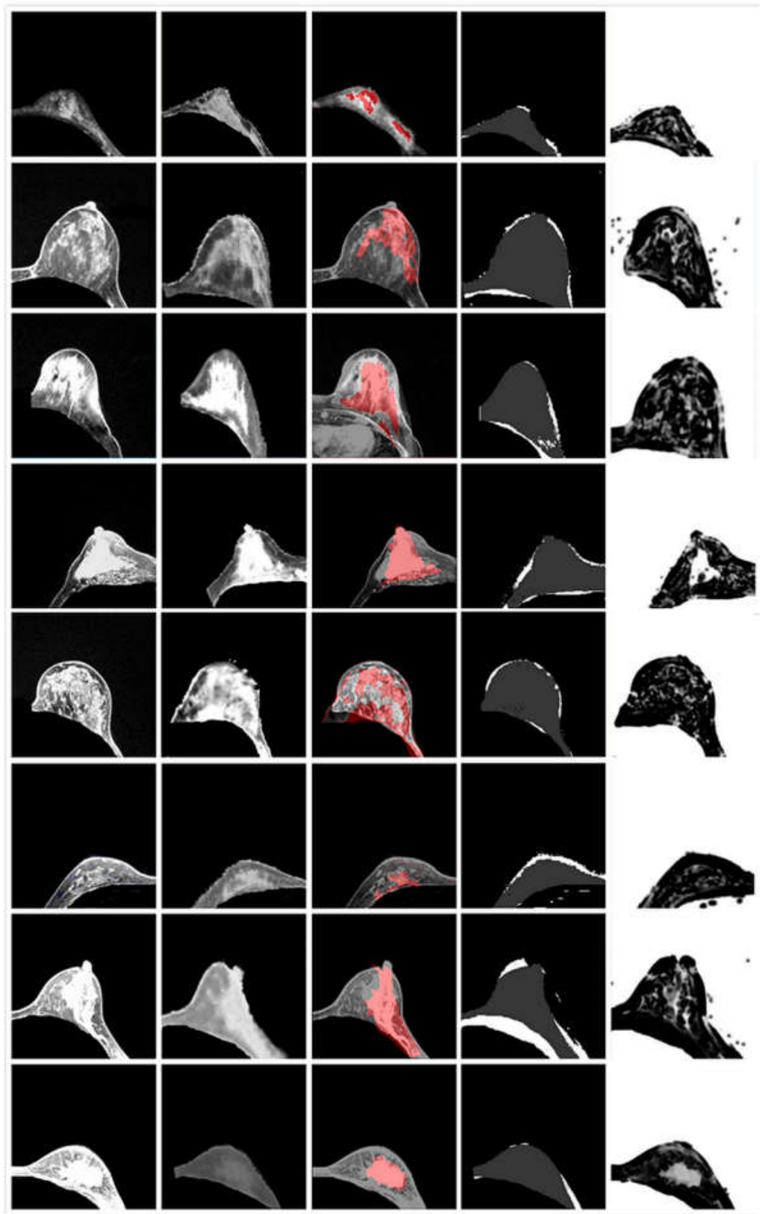

Figure 4.8 Registration performance. First column: real MR images in prone position. Second column: predicted CT images in prone position. Third column: registered MR/CT images, fibro-glandular tissues colored in red. Fourth column: overlapping images that compare contours of predicted CT images with real MR images. Last column: mapping of local SSIM values.

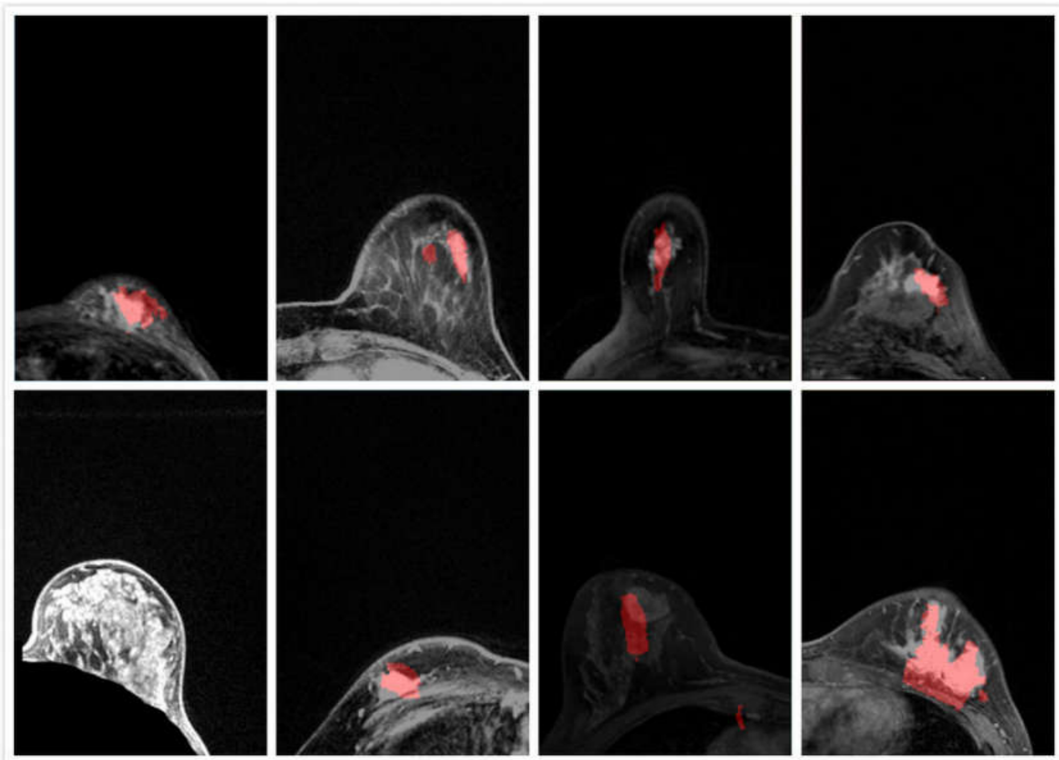

Figure 4.9 Registered PET/MR images. Lesions in PET images colored red.

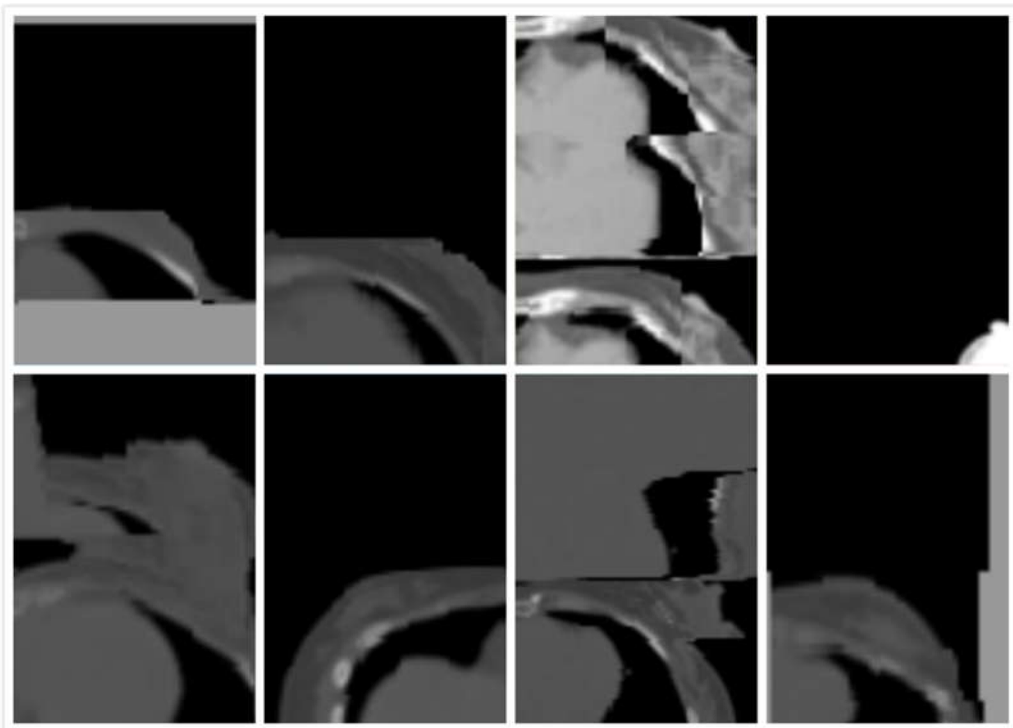

Figure 4.10 SIFT registration of PET and MR images: incompletion of registration due to large deformation of breast.

4.3.2 Evaluation

As mentioned before, there is no universal consensus for evaluating image registration. Therefore, six parameters are proposed in this study to evaluate the established process. The parameters and their mean values, standard deviations (SD), and SD/mean are presented in Table 4.3.

Table 4.3 The evaluation matrix. (mutual information (MI), correlation ratio (CR), image structural similarity index (SSIM), dice coefficient (DICE), and target registration error (TRE and TRE_{rel}.)

Case No.	MI[a]	CR[b]	SSIM[c]	DICE[d]	TRE (g) /mm[e]	TRE_{rel} (g)[f]	tre(l) /mm	tre_{rel}(l)	DICE(l)
H1	0.491	0.744	0.894	0.842	5.98	0.145	4.47	0.121	0.721
H2	0.965	0.705	0.696	0.939	9.93	0.162	2.23	0.151	0.644
H3	0.675	0.840	0.759	0.890	13.1	0.165	2.67	0.112	0.556
H4	0.594	0.907	0.829	0.921	9.27	0.083	6.71	0.367	0.468
H5	0.574	0.739	0.767	0.903	2.51	0.017	NA	NA	NA
H6	0.373	0.831	0.810	0.841	8.83	0.162	4.06	0.135	0.641
H7	0.539	0.817	0.750	0.782	12.604	0.075	9.04	0.402	0.464
H8	0.466h	0.319	0.839	0.867	8.01	0.116	4.24	0.069	0.668
Mean	0.585	0.738	0.793	0.873	8.27	0.1156	4.77	0.19	0.59
SD	0.166	0.169	0.058	0.047	2.87	0.049	2.20	0.12	0.09
SD/Mean	0.285	0.229	0.07	0.05	0.35	0.0438	0.45	0.64	0.16

[a]MI is the mutual information.
[b]CR is the correlation ratio.
[c]SSIM is the image structural similarity imdex.
[d]DICE is the dice coefficient.
[e]TRE is the target registration error.
[f]TRErel is the relative target registration error.

The MI, CR, SSIM, and DICE values range between zero and one. MI has the lowest value of 0.585±0.166. The average CR, SSIM and DICE is all greater than 0.7, which indicates that the predicted image has a good overall performance. The TRE(g) of the fibro-glandular tissues is 8.27±2.87 mm, and $TRE_{rel}(g)$ is 0.116±0.049 mm. The TRE(l) of the lesion is 4.77±2.19 mm, which is only about 3 pixels in an MR image (resolution:1.3 pixels per mm). The DICE and $TRE_{rel}(l)$ of the lesion is 0.59±0.09, and 0.19±1.12 respectively.

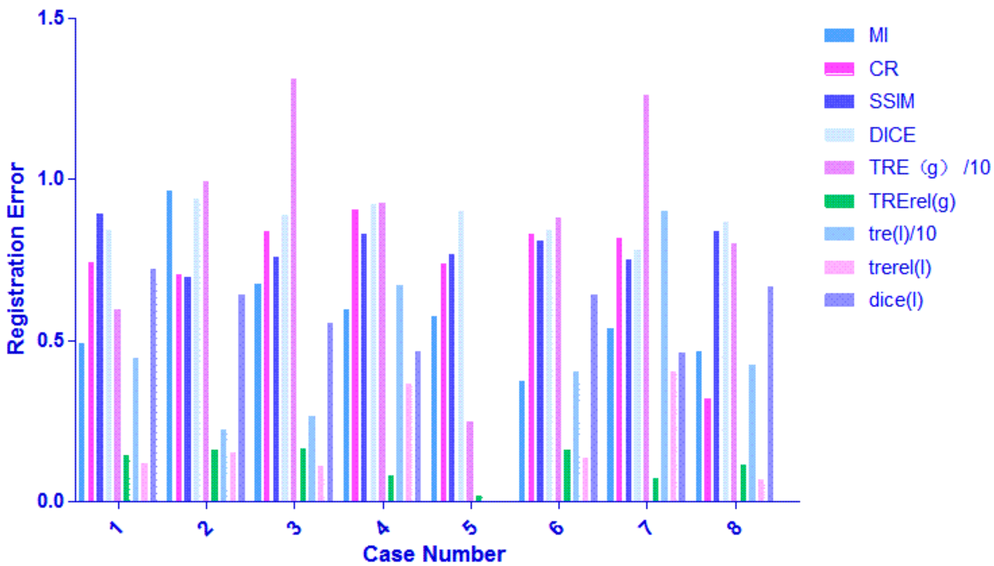

Figure 4.11 Case registration errors: MI, CR, SSIM, DICE(g), TRE(g), TRE_{rel}(g), DICE(l), TRE(l), TRE_{rel}(L). MI, CR, and SSIM: errors for overall image performance. DICE, target registration errors of landmarks (TRE(g) and TRE(l): registration performance of internal features.

To determine the correlation between the six parameters, Pearson's correlation coefficient (R) was calculated for all of the parameters. Parameters with a higher R-value are shown in Table 4.4, along with the correlated parameters and their significance. It can be observed that MI is negatively correlated with SSIM ($R=-0.7216$, $p<0.05$). $TRE_{rel}(l)$ and Dice(l) are negatively correlated ($R=-0.8626$, $p<0.05$).

Table 4.4 Parameters with high correlation coefficient.

Pearson's correlation coefficient			
MI	SSIM	-0.7216	0.0432
$TRE_{rel}(l)$	Dice(l)	-0.8626	0.0125

4.3.3 Dataset analysis

To determine whether the image features can predict the simulation performance (TRE of the fibro-glandular tissues and lesion) before registration was conducted, six image features (image density, breast volume, patient age, distance of lesion from the chest wall, and diameter of lesion) were extracted from the CT and PET images, and plotted in Figure 4.12. The correlation coefficient was calculated between TRE and each feature. However, no correlation was found.

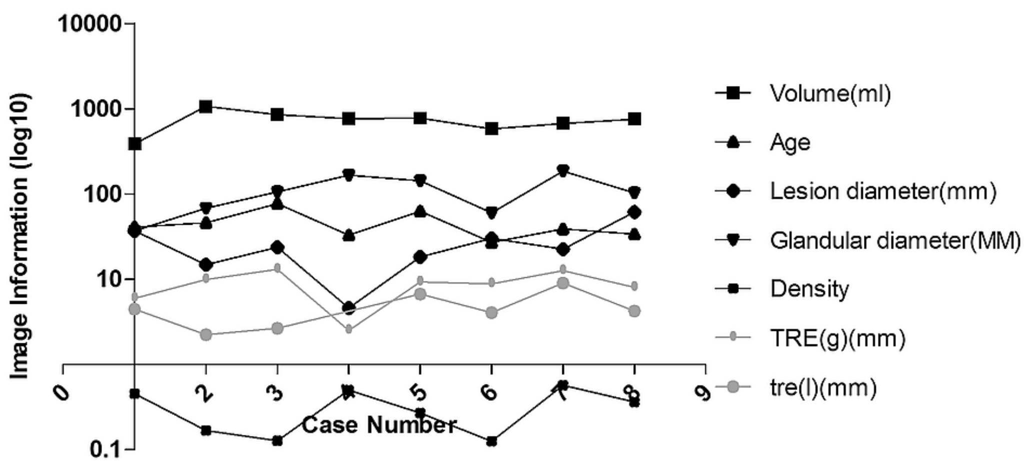

Figure 4.12 Plotting of image features vs. TRE (TRE(g) of fibro-glandular tissues and TRE(l) of lesion colored gray). No correlation found.

4.3.4 Mechanical properties

In this section, an inverse FEA and optimization process were combined to predict the elastic properties of the adipose and fibro-glandular tissues. This method can predict the mechanical properties, which may not necessarily be a real value, but provide an overall trend.

The predicted moduli of the breast tissue compared with the values found in the literature are listed in Table 4.5. It can be observed that the range of material properties predicted in this study is smaller than the range predicted by Roose, Tanner and Gefen. The material properties range of this study is close to the properties predicted by Guillaume.

Table 4.5 Predicted moduli of breast tissue compared with values in literature.

Young's modulus (kPa)	**Roose (2005)**	**Tanner et al. (2006)**	**Gefen and Dilmoney (2007)**	**Guillaume et al. (2013)**	**Study results**
Glandular	1.7-500	1-20	7.5-66	0.5-10	3.75-39.2
Adipose	1.7-500	1	0.5-25	0.1-2	0.5-5.2

4.4 ***Discussion***

4.4.1 Modeling process

In this chapter, I have presented a hybrid approach to register MR images in the prone position and PET/CT images in the supine position. Large deformations were firstly simulated by using FEM, with 3D/3D surface-based registration. The structure and mechanical properties of both the fatty and fibro-glandular tissues were taken into consideration. Then, affine transformation was applied to the deformed image to complete the hybrid registration.

An iteration process to optimize the Young's modulus was integrated into the method. To determine the mechanical properties that were to be optimized, the impact of the values of the Poisson's ratio, Young's modulus, and density was calculated respectively. The impact of the Young's modulus and density is greater than that of the Poisson's ratio. However, most materials with a higher density have a higher Young's modulus, so only that Young's modulus of the fatty and fibro-glandular tissues was optimized. The optimization process of the Young's modulus stopped when the difference between the simulated and actual nipple displacements was within 1 mm, and no extra calculations were needed. Han et al. calculated normalized mutual information as the terminating condition (Han et al., 2014). As FEA was used to simulate the deformation process, deformation used as the terminating condition of optimization provides a better quality optimization; therefore, nipple displacement rather than intensity based parameters was used as the optimization criterion.

4.4.2 Performance analysis

Different images from the same object with different spatial information can be registered by using SIFT registration. SIFT registered MR and PET images are therefore used for comparison purposes in this study. However, the resolution of the PET images was too low for SIFT registration to obtain the spatial information, and the deformation of the breast was too large, so registration by using SIFT could not be completed.

In clinical practices, image registration can help radiologists to more readily identify lesions. The parameters used to assess the image registration, MI, CR, TRE, SSIM, DICE and TRE_{rel}, were therefore used. In thesis evaluation metrics, the parameters with the highest average mean value is DICE (0.873±0.047).

The Pearson's correlation coefficient of all of the parameters were calculated in the evaluation matrix. The parameters with high correlation (p<0.05) are shown in Table 4.4. MI and SSIM were found to be negatively correlated. TRE_{rel}(l) and DICE(l) were found to be negatively correlated, which shows that when using smaller sized landmark, DICE is another parameter that can be used to evaluate the performance of the registration.

A comparison between the method in this study and that of previous studies is shown in Table 4.6. The TREs of both the fibro-glandular and fatty tissues with the use of the method proposed in this study are lower than those of earlier studies. The overall image similarity of the eight image sets in this study is 0.793±0.058, which also indicates that the rebuilt images of deformation have high similarities with the MR images.

The highly accurate registration indicates that the established mechanical model of the breast in this study can simulate deformations of the breast from the supine to prone positions. This proposed model also addresses patient-specific properties of the human tissues. The application of this model is not restricted to image registration. It can also be used to enhance image-guided surgery and plastic surgery of the breast, as well as medical device development.

Table 4.6 Comparison of target registration errors.

<table>
<tr><th>Registration error</th><th>Method in this study</th><th>Han et al. (2012)</th><th>Hopp et al. (2013)</th></tr>
<tr><td>TRE(g)/mm</td><td>8.27±2.87</td><td rowspan="2">9.86±2.77</td><td rowspan="2">11.0±8.3</td></tr>
<tr><td>TRE(l)/mm</td><td>4.77±2.20</td></tr>
<tr><td>$TRE_{rel}(l)$</td><td>0.19±0.12</td><td></td><td>0.73±0.90</td></tr>
</table>

4.5 *Conclusion*

A patient-specific biomechanical model of the breast has been established in this study. A 3D breast model is formulated with sufficient meshes and a smooth surface in a very convenient way in comparison to previous studies. This method uses ABAQUS software which can reduce the time demand for modeling and increase accuracy at the same time.

Eight sets of images are used to evaluate the proposed model. The average TRE of the fibro-glandular tissues in the images is 8.27±2.87 mm, and 4.77±2.20 mm for the lesion, with an overall image similarity of 0.738±0.169. The performance of this model excels that of previous studies. The advantage of using this method is that applications are not limited to PET/MR image registration, but any deformation in the supine to prone positions. This established patient-specific mechanical model can accurately register the breast from the supine to prone positions and help with the early detection of breast cancer, and also has the potential to improve radiotherapy planning.

5 Images from two institutions for model validation

5.1 *Introduction*

A biomechanical model that can accurately reflect the deformations of the breast in the supine to prone positions has been established (see Chapter 4). In reflecting the deformations, clinicians can better analyze the images and make appropriate diagnoses.

However, the breast size of Asian and Caucasian women is usually different because of their different diets and genetic variants, and fat/glandular tissue composition, and contouring of breast. Normally, Asian women have smaller, denser breasts than Caucasian women (Nie et al., 2010).

To identify whether the model developed in this study is applicable to patients with different breast size and of different race, 20 additional sets of images were collected from an American institution.

5.2 *Method*

As the density and volume may affect the performance of the proposed biomechanical model of the breast. To identify this, twenty more PET/CT and matching MR image sets were collected from Duke University Health System in USA (GE Discovery STE and Siemens Avanto). The scans were acquired within 6 months of each other as part of routine clinical practice. The breast volume was measured from the 3D CT model. Two pairs of images (D19 and D20) were excluded from the former because the deformation was extremely large so that contact was made with the breast MR coil (as shown in Figure 5.1). Thus, the deformation of the breast is not only a result of gravity but also the holding force from the coil. However, this is not the scope of this study. In the evaluation stage, one pair of breast images from the Hong Kong sample (H5) was excluded, because there is no clear cancer lesion in the MR image that can be used to perform evaluation. Therefore, a total of 25 image sets (both PET/CT and MR) are used to evaluate the model. The information of the images are shown in Table 5.1. The volume and density of these cases are plotted in Figure 5.2.

Table 5.1 Information of the US patients.

Case No.	Lesion size (mm)	Volume (ml)	Density	Nipple displaceme nt (mm)	Weight (kg)
D1	22.7	687	0.17	82	51.7
D2	23	1584	0.10	79	77.1
D3	24.4	408	0.38	77	58
D4	24.8	601	0.20	35	52.6
D5	46.5	2476	0.10	138	99.7
D6	36.2	742	0.16	60	74.8
D7	4.7	493	0.17	40	58
D8	14.5	597	0.25	75	56.7
D9	18.1	924	0.49	103	74.8
D10	66.6	1948	0.12	65	115.6
D11	64.9	1442	0.26	122	73
D12	11.7	918	0.14	90	77.6
D13	15.7	1078	0.12	65	66
D14	48.9	566	0.07	61	62.6
D15	19	1055	0.08	75	95.3
D16	38.2	3779	0.03	118	113.4
D17	12.8	597	0.24	70	54
D18	41	1728	0.03	118	113.4

The breast volume of the American sample was compared with that of the Hong Kong sample. As shown in Table 5.2, the median of the breast volume of the former is 990ml, the density has a median value of 0.15. The median value of the breast volume of the latter is 762ml, the median value of density is 0.27. The density of the American sample is significant smaller than that of the Hong Kong sample ($p<0.05$). It is hypothesized that the volume size and density may affect the performance of the mechanical model of the breast developed in this study. To determine whether this is true, the correlation coefficient values were calculated.

Figure 5.1 Excessive deformation in excluded MRI image.

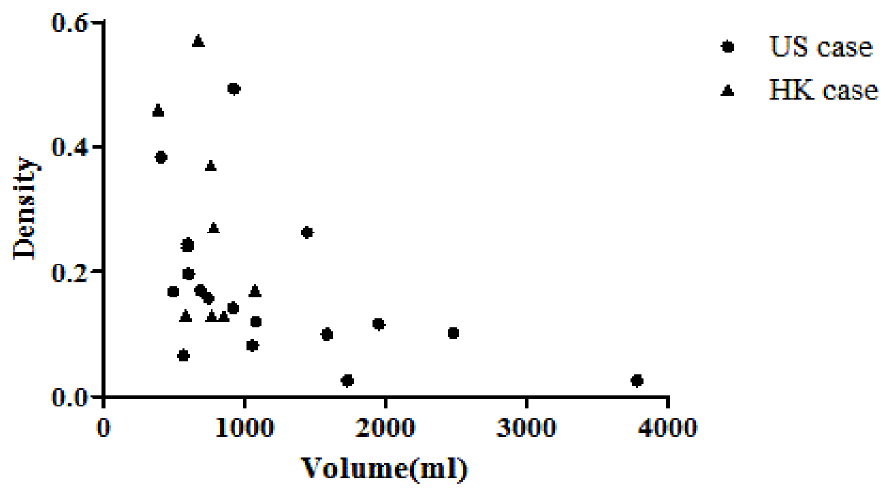

Figure 5.2 Scatter plot of volume vs. density.

Table 5.2 Comparison of breast volume and density: American vs. Hong Kong women

	American	Hong Kong
Median of breast volume (ml)	990	762
Median of breast density	0.15	0.27

5.2.1 *Modeling*

Following the same modeling method provided in Figure 4.1, eighteen more 3D models were created. First, all of the CT images were cropped in accordance with the location of the lesion. Then the images were segmented into the adipose and fibro-glandular tissues by using a fuzzy-c means algorithm. The 3D modeling of the fatty and fibro-glandular tissues was based on the segmented CT images respectively. The skin was modeled by adding an extra 1 mm layer of mesh onto the surface of the breast model. The material properties and boundary conditions obey the same rules as mentioned in Section 4.2.2. The adipose tissues and skin were assigned a density of 1000 kg/m^3 and fibro-glandular tissues a density of 1200 kg/m^3. Both the adipose and fibro-glandular tissues obeyed the Neo-Hookean constitutive relationship. Two landmarks were recognized in the PET/CT images, which is the nipple in the CT image and lesion in the PET image. Since the lesion is used as a landmark for the evaluation of registration error, nipple displacement was used as the standard to optimize the model. Nipple displacement in the supine to prone positions was calculated by using rigid pre-registration for each image pair. After the first round of FEA, the nipple displacement was compared with that of the calculated displacement. The material properties of the fatty and fibro-glandular tissues were determined through an exhaustive search to minimize the nipple displacement differences. After completing the optimization, the optimized node displacement was exported to interpolate with the pixel value of the PET image and form a PET image of the deformation.

The specific steps in ABAQUS software are: input model, assign material properties, and cut the model into little cube, generate meshes, assign boundary conditions and loading, the last step is analysis.

5.2.2 Affine transformation and registration

Intensity based registration has been widely used in medical image registration. Nevertheless, for objects that have large-scale deformation, it is difficult to complete the combining of images based on only intensity. However, if the image is deformed before intensity based registration is conducted, the accuracy will greatly increase. Therefore, FEA can provide the basis for intensity based registration.

Affine transformation was applied along with FEA because, first of all, affine transformation is easy to apply. Also, affine transformation does not overly depend on image intensity, as PET images are low in resolution.

To simplify the registration process, in contrast to Chapter 4, registration was directly applied to PET and MR images in this chapter. CT images were used in Chapter 4 because some evaluation metrics such as mutual information, correlation ratio and SSIM can only be calculated based on CT image or MR image. But TRE is found to be the main metric used in the evaluation process, therefore, only TRE is needed in this chapter. This means only register PET with MRI is enough in this chapter. The landmarks used to calculate the transformation were three points on the contours of the chest wall. These three points were manually selected according to the shape features. This transformation was then applied to the PET images to generate new deformed PET images. The new images were then overlapped with MR images to complete registration. The lesion in the PET images was also colored in red so that it can be readily identified.

5.2.3 Machine learning

Generally, machine learning is a process that analyzes data from different perspectives, categorizes the data, and summarizes the data to extract useful information. The purpose of machine learning is to extract information based on various rules and transform this information into a comprehensible structure.

In this section, I used an open source data mining software WEKA (Hall et al., 2009) to determine the means to classify the data based on the extracted features, so that the registration accuracy can be predicted before registration takes place.

Cross validation (Picard & Cook, 1984) is a process in which the data are split into two parts. One part is used as the training set to fit the model and another part is used for validation.

The features that were extracted from the images include: patient weight, lesion size, nipple movement displacement, location of lesion, image density, and breast volume. The location of the lesion is defined as a ratio of the distance of the lesion to the chest wall over the distance of the farthest vertices to the chest wall. When the lesion is near the chest wall, this value is close to zero. When the lesion is near the surface of the breast this value is close to one.

5.3 ***Results***

5.3.1 Model performance

Two random chose pairs (case D6 and case D11) of the predicted deformed breast models before affine transformation and real breast models of the prone position are shown in Figure 5.3. The pink colored model is formulated based on MR images in the prone position and the green colored model is the predicted CT breast model in prone position. The blue colored model from the corresponding CT images in the supine position. The difference between the CT images in the supine position (e), (j) and the MR images in the prone position (b), (l) is extremely large, which means that simulation of the deformation is quite difficult. The predicted model for the prone position (c, d), (h, i) and real model of the prone position (a, b), (f, g) in the superior-inferior and lateral-medial directions were compared. It was found that the performance of the developed model is good enough to predict a general deformation of the breast.

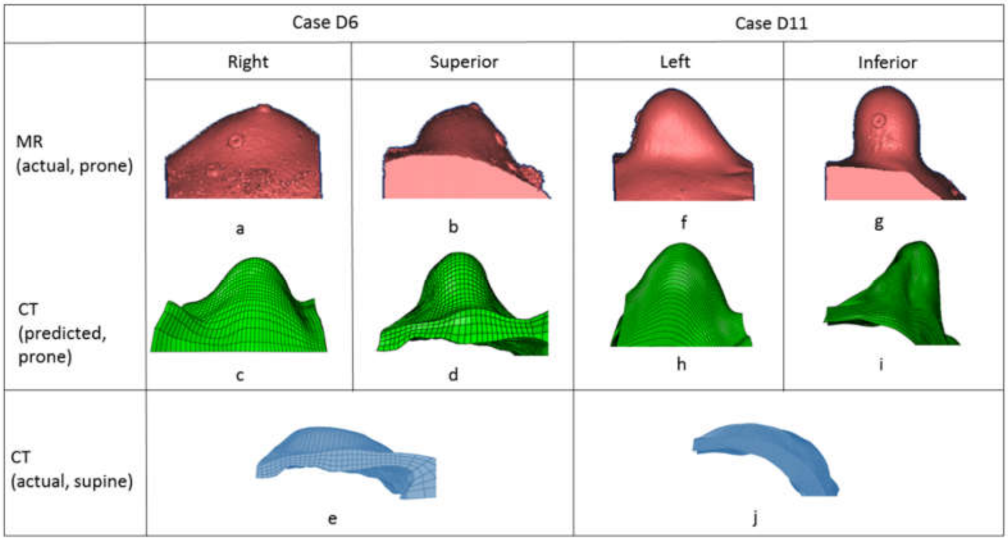

Figure 5.3 Comparison of predicted (green; (c,d,h,k)) and real (pink, MR images) breast models in prone position. Breast model in supine position (e and j; CT images).

5.3.2 Registration error

An evaluation matrix with six parameters (mutual information (MI), correlation ratio (CR), structural similarity index (SSIM), dice coefficient (DICE), target registration error (TRE) and the measured relative error of the target registration (TRE_{rel})) was provided in Chapter 4. However, due to the low resolution of PET images, MI, CR, DICE and SSIM are not available. Therefore, only TRE of the lesion was calculated and discussed in this chapter, the TRE in this chapter represents TRE of the lesion.

The TRE of the lesion was calculated with 3D coordinates, rather than in a 2D plane. The target registration error of the lesion was calculated in three-dimensional coordinates, rather than within a 2D plane. The value of 3D TRE is provided in Table 5.3, with a mean value of 8.05 mm and a SD of 6.6 mm. According to the Breast Imaging Reporting and Data System (BI-RAD), the 25 cases were divided into low density group (LD) and high density group (HD) with a threshold of density equal to 25%. The median value of volume was used as the threshold that divided all the cases into small volume group (SV) and large volume group (LV). The TRE value in LD group is significantly smaller than the HD group (unpaired t test, $p<0.05$). However, there is no significant difference between SV and LV group, and the US and HK group (Figure 5.4). The predicted location of the lesion compared to use of the MR images is shown in Figure 5.5. The lesion in the PET images is red in color.

The TRE of the US cases range from 3.11mm to 34.18mm, with a mean value of 9.14mm and a SD of 7.41mm. The TRE value of the HK cases is 5.17±2.34mm.

Three random chose registered images are shown in Figure 5.6, with green representing deformed PET images and purple representing the MR images. It can be observed that with the use of the deformed PET images, the location of the lesion can be accurately predicted. The registered PET/MR images provide detailed structural information as well functional information on the lesion.

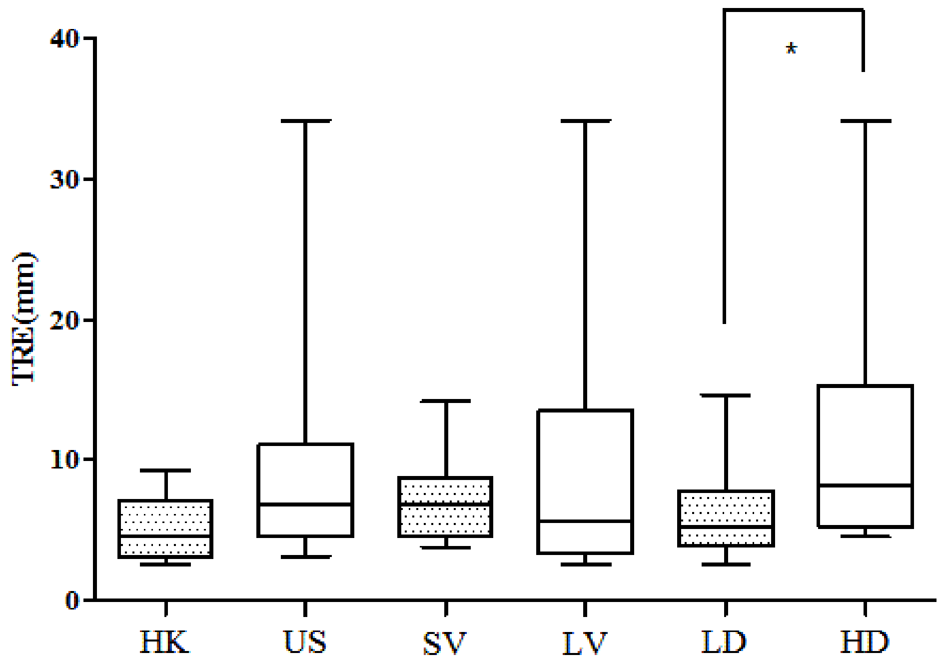

Figure 5.4 3D TRE compared between HK and US group, 3D TRE compared between small volume (SV) group and large volume (LV). 3D TRE compared between low density (LD) group and high density (HD) group. No significant difference was found in the last two group.

Table 5.3 Registration accuracy and patient-specific information extracted from image.

Case No.	Lesion size (mm)	Lesion location	Volume(ml)	Density	Nipple displacement (mm)	Weight (kg)	TRE (mm)	Accuracy
D1	22.7	0.14	687	0.17	82	51.7	6.88	good
D2	23	0.02	1584	0.10	79	77.1	3.84	good
D3	24.4	0.41	408	0.38	77	58	15.12	suboptimal
D4	24.8	0.48	601	0.20	35	52.6	8.02	good
D5	46.5	1.41	2476	0.10	138	99.7	5.22	good
D6	36.2	0.48	742	0.16	60	74.8	10.09	good
D7	4.7	0.39	493	0.17	40	58	3.77	good
D8	14.5	0.48	597	0.25	75	56.7	6.89	good
D9	18.1	0.30	924	0.49	103	74.8	15.71	suboptimal
D10	66.6	0.69	1948	0.12	65	115.6	7.60	good
D11	64.9	0.43	1442	0.26	122	73	34.18	suboptimal
D12	11.7	0.12	918	0.14	90	77.6	5.31	good
D13	15.7	0.31	1078	0.12	65	66	14.64	suboptimal
D14	48.9	0.32	566	0.07	61	62.6	4.69	good
D15	19	0.45	1055	0.08	75	95.3	5.92	good
D16	38.2	0.25	3779	0.03	118	113.4	3.11	good
D17	12.8	0.15	597	0.24	70	54	3.91	good
D18	41	0.79	1728	0.03	118	113.4	10.03	good
H1	37	0.30	386	0.46	31	70	4.58	good
H2	14.8	0.81	1072	0.17	69	68	2.53	good
H3	23.8	0.64	852	0.13	93	65	3.03	good
H4	18.3	0.70	776	0.27	39	60	7.13	good
H6	30.1	0.44	582	0.57	27	60	5.17	good
H7	22.5	0.79	670	0.36	18	75	9.26	good
H8	61.3	0.42	757	0.46	29	65	4.5	good

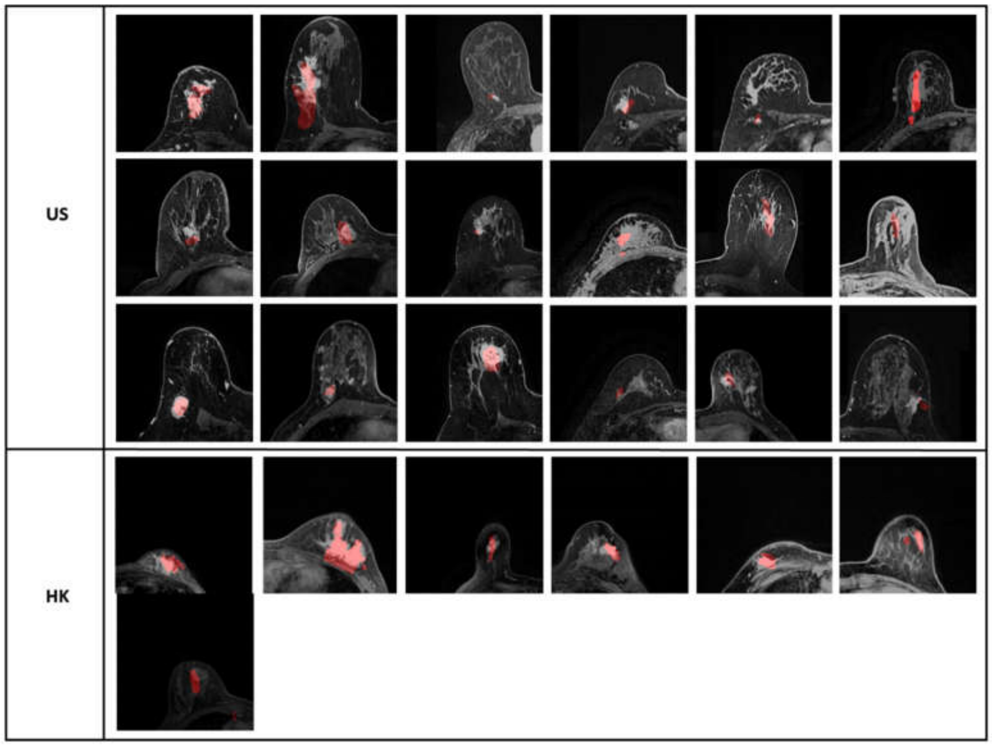

Figure 5.5 Predicted lesion location. Lesion from PET image in red.

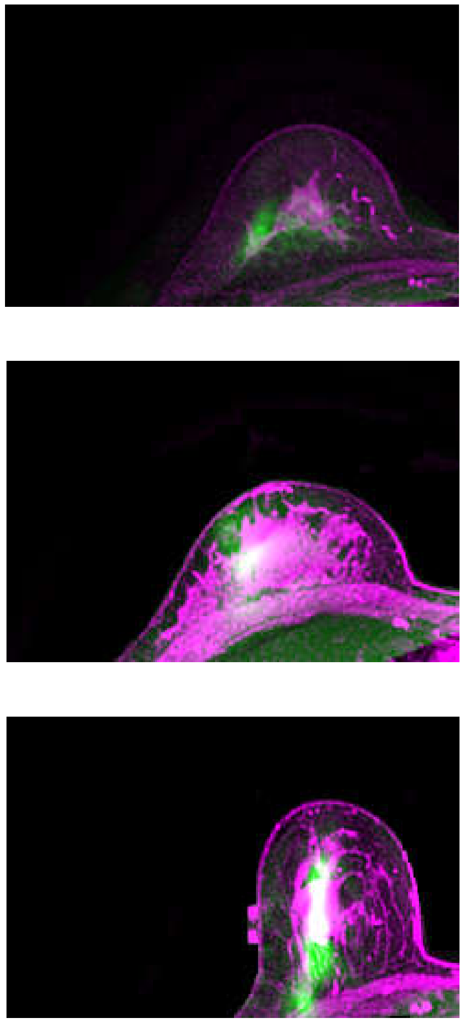

Figure 5.6 PET/MR registered images: MR image – purple; PET image - green; image overlapping - white.

5.3.3 Correlation analysis

Six image features extracted from the PET/CT images and the TRE were plotted to identify their relationships. However, no correlation was found when plot the HK cases and the US cases together. While, the density and TRE of the HK case has a correlation of 0.67, but due to the small sample size of HK cases, this correlation is not significantly. The density of the US case was found to be correlated with the TRE value in all the 18 cases ($R=0.47$ $p<0.05$). However, other features include the volume did not show any significant correlation with TRE. The TRE and corresponding density are plotted in Figure 5.7.

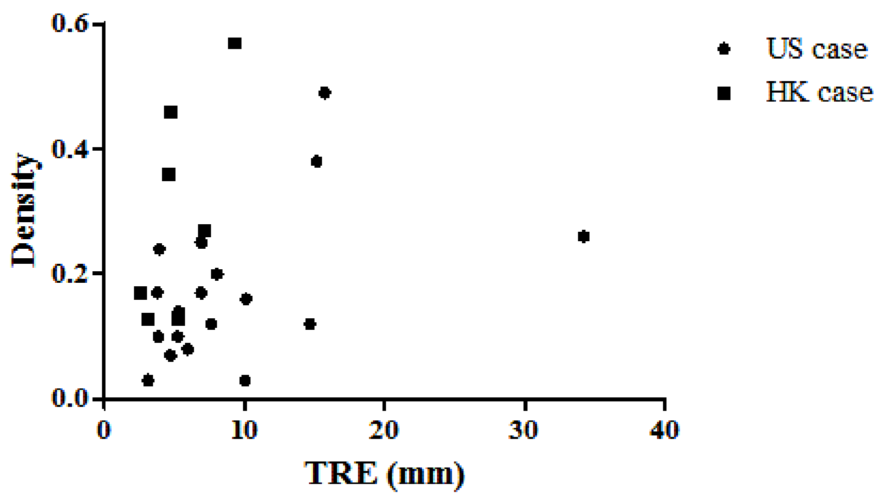

Figure 5.7 TRE vs. density.

5.3.4 Prediction of registration accuracy

The registration accuracy classification was predicted by the six image features using logistic regression. According to the mean value of TRE, the registration error was classified as having good accuracy with a TRE less than 10 mm, and a suboptimal accuracy with a TRE greater than 10 mm for all the US cases, the threshold of HK group was set as 6mm. The results showed that for the American sample (18 cases), there are 66.7% correctly classified instances with a sensitivity of 62% and a specificity of 65.1%. For Hong Kong sample, there are 71.4% correctly classified instances with a sensitivity of 90% and a specificity of 92.9%.

5.3.5 Mechanical properties

The predicted moduli of the breast tissue in the American sample are between 0.5-1.7 kPa for the adipose tissue and 3.75-12.75 kPa for the fibro-glandular tissue. It is 0.5-5.2 kPa for the HK adipose and 3.75-39.2 for the HK fibro-glandular tissue as shown in Table 5.4.

Table 5.4 Comparison of predicted moduli of breast tissue compared with values in literature.

Young's modulus (kPa)	**Roose (2005)**	**Tanner et al.(2006)**	**Gefen and Dilmoney (2007)**	**Guillaume et al. (2013)**	**This method**
Glandular	1.7-500	1-20	7.5-66	0.5-10	3.75-39.2 for HK case 3.75-12.75 for the US case
Adipose	1.7-500	1	0.5-25	0.1-2	0.5-5.2 for HK case 0.5-1.7 for the US case

5.4 *Discussion*

The model that was formulated in Chapter 4 has been evaluated with an additional 18 cases from the Duke University. The most significant difference is that the breast density is different amongst the images. The breast images collected from the American sample of women show much lower breast density than those of the Hong Kong sample ($p<0.05$). This is the first study according to our knowledge that images from more than one ethnic group are used to evaluate a biomechanical model. The versatility of the model is therefore validated.

The TRE is 77% greater than that of the Hong Kong case in Chapter4, but still demonstrates a good result compared to previous studies (see Table 4.6). The reason might be due to the shape of the breast in the supine position. In some cases, the breast sags towards the abdomen which makes the modeling difficult. This may have effects on the deformation performance. Another reason might be the volume and density of the breast, which differs between the American and Hong Kong samples. In addition, I have found that the density is correlated to the TRE ($R=0.47$, $p<0.05$). Moreover, the TRE in the low density group is significantly smaller than the high density group. This indicates that the developed biomechanical model in this study can more accurately predict the deformation of breasts with less density. Even though, the TRE of the American sample is greater than that of the Hong Kong sample, but still demonstrates a good result compared to previous studies (Han et al., 2014; Hopp et al., 2013). The TRE in Han's study is 9.86±2.77 mm (Han et al., 2014), the TRE of a compression model by Hopp et al (Hopp et al., 2013) is 11.0±8.3 mm (in XY domain), and the TRE of our method (8.05±6.60 mm) is smaller than these two studies. The sample size in this study is 25 in total, while Han's has eight samples and Hopp's has 79 datasets, our sample size is smaller than

Hopp's. But our study collected samples from two institutions on two countries. As shown in Table 5.3, the highest TRE value is Case 11. According to the prediction of the lesion as shown in Figure 5.5, the lesion is blurred. This blurred lesion can lead to large errors. When Case 11 is excluded, the TRE is 6.95±3.81 mm, which is 14% smaller.

The range of the predicted moduli of the breast tissue of the American sample is slightly less than that of the Hong Kong sample, which is 0.5-1.7 for the adipose tissue.

Data mining has also been applied to classify the features that were extracted from images in a way that can be related to the TRE. The results showed 88.9% correctly classified instances with a sensitivity of 73.2% and a specificity of 80.8%. However, this ratio is also dependent on the standard used to determine the performance of the registration. In this study, a TRE greater than 11 mm is considered suboptimal. However, if the standard is changed, the ratio will also change.

Therefore, if data mining is used to predict registration errors, a criterion must be developed to denote the level of accuracy.

5.5 *Conclusion*

This chapter focuses on evaluating the established biomechanical model. Twenty cases from an American sample have been collected but two excluded. The registration error is 77% higher than that of the Hong Kong sample, but still has a relatively low mean TRE. The TRE is found to be correlated to the image density. Logistic regression shows that the six image features can predict the registration error.

In conclusion, this developed model can accurately predict the deformation of the breast from the supine to prone positions for both the Hong Kong and the American samples by logistic regression.

6 Conclusions and recommendations for future work

6.1 *Summary of thesis*

The overall goal of this thesis is to develop a mechanical model of the breast that can be used to assist with clinical diagnoses and treatment. In addition, the model will aid clinicians in reading the breast images derived from multiple modalities. A biomechanical model of the breast has therefore been developed and used to simulate the deformation of the breast under gravity from the supine to prone positions. In this thesis, FEA and affine transformation are integrated to develop a registration framework. The model is validated by using twenty-five MR and PET/CT images of breasts collected from both the Hong Kong and American samples, which means that this model is evaluated by using the data of both Asian and American women. The accuracy for both samples is very high. A correlation between density and TRE has been identified, which can be used to predict the performance of deformation simulation and accuracy of registration before the analysis is conducted.

6.2 *Modelling gravity-induced deformations*

In this study, an approach to formulate a mechanical model for breasts is presented to determine the possibility of whether a finite element model can accurately simulate large-scale deformation induced by gravity. The parameters that need to be taken into consideration have been identified during the building of the model. A good number of images are used to construct the model. In this study, a larger database is used as opposed to that in previous studies.

A method to construct a finite element model of the breast which can simulate deformation is proposed in Chapter 3. This model is constructed from CT images of patients in the supine position. Since gravity already acts on the breast when the images were acquired due to the position of the patient, the initial loading environment has to be taken into account during the simulation. This initial loading is considered by determining a reference state with no internal stress, which means a state that has no loading applied onto the breast model. Three ways as mentioned in Section 3.3 are discussed to calculate the reference state. I have chosen an effective way, which is very common in engineering, which can be finished by ABAQUS.

In Chapter 3, I also considered the effect of many parameters on the simulated deformation because there is a tradeoff between the mesh size and efficiency. Apparently, a smaller mesh can lead to higher accuracy, while also increasing the time needed to finish the analysis. The mesh size is determined by testing the mesh sensitivity and computation time. Finally, a mesh density of 60 elements per unit area is used. To choose a mesh type from the tetrahedron and hexahedron shapes, I have calculated the computation time for both mesh types. The computation time for a hexahedral mesh is less when the mesh size is the same for both meshes. Thus, a hexahedral mesh is used in this study to build an FE model of the breast.

When CT/PET images of a patient are captured in the supine position, the patient may be in the same position for a long time. Therefore, the volume of the breast might have changed due to the changes in the fluid content with time. Consequently, I compared the effect of different Poisson's ratios. The Poisson's ratio is usually 0.45-0.49 due to the incompressibility of the breast. On the examined cases in this study, I have found that the volume of the breast in the supine to prone positions does not change very much, which is in agreement with the fact that the breast is incompressible. The Poisson's ratio is therefore assigned a value of 0.45.

I have also described the preparation of breast imaging processes in Chapter 3, and the most important component in building a patient-specific breast model is to segment the breast image. In this study, I have evaluated three image segmentation methods to segment the CT images used for breast modeling. Given its efficiency and accuracy, I have chosen the fuzzy-c means algorithm for segmentation, which can clearly and quickly locate the adipose and glandular tissues.

6.2.1 Registration of CT/PET and MR images in supine and prone positions

The PET/CT images of the breast are acquired in the supine position, while the MR images in the prone position. However, the latter can provide more details on the breast features and deformation. In order to align the PET and MR images together, the PET images are combined with the MR images.

In Chapter 4, I discuss the entire process of building a mechanical model for the breast. Moreover, the model is applied to complete the registration of breast images taken from multiple image modalities. The entire process is semi-manual, so that the chest wall can be manually excluded from the final image.

The model developed in Chapter 4 can be used as the basis for a registration method. Intensity based registration methods can be realized after applying this deformation approach to further complete registration. I have tried SIFT-based registration to align images in the supine and prone positions, which does not work. The problem could be that the initial overlapping region is too small and the structural information in CT images is quite limited.

The most important part of the whole process is the optimization process. I have identified the proportion of Young's modulus, density and Poisson's ratio, which is 0.7, 0.6 and 0.1 respectively. As the Young's modulus and density are somewhat related, only Young's modulus is optimized in this study. The optimization criteria are spatial information (nipple displacement) that is different from that in previous studies. The TRE for the lesion in this study is 4.77±2.19 mm, which is very good.

In Chapter 4, I have also used six evaluation standards to formulate an evaluation matrix, which contains MI, CR, SSIM, DICE, and TRE and TRErel. However, only DICE is correlated with the TRE of the lesion.

To further evaluate the possibility of the model to predict breast deformation, six features of the patients, namely, image density, breast volume, patient age, distance of lesion from the chest wall, and diameter of lesion, are extracted from the images. However, as the sample number is small, no correlation is found.

6.2.2 Evaluation of established model: American vs. Hong Kong samples

In Chapter 5, I used additional images taken from the American sample to evaluate the model. Some improvements are made, 3D TRE was calculated, and registration was processed on PET and MR images directly. The focus is mainly on evaluation and data analysis. The image density is found to be correlated with TRE ($R=0.47$, $p<0.05$). The TRE of the lesion is 8.05 ± 6.60 mm. This suggests an overall registration accuracy that ranges between 2.50 mm and 34.18 mm.

By using machine learning, I find that the six images features can be used to predict the registration error before conducting the registration.

6.3 ***Future directions***

In this study, I have established a patient-specific biomechanical model that can simulate breast deformation from the supine to prone positions. The model is evaluated by comparing the registration of breast images between the supine and prone images. The standard used to validate the quantitative data is the measurement of the TRE. Twenty cases collected from the Duke University are processed to evaluate the established model. However, further studies should focus on improving the sensitivity and applicability of the model in clinical settings.

6.3.1 Improvement of modeling

To improve the robustness and reliability of the modeling, the boundary conditions in the FEA can be optimized by adding a sliding boundary condition along the chest wall. A more detailed model can thus be constructed by including Cooper's ligaments and muscles to better simulate the movement of the breasts.

As I have simulated the supine to prone positions in this thesis, future studies can consider the establishing of a general model that can be used to simulate the deformation of the breast with any movement, such as prone to supine, and compression. The studies can focus on the boundary conditions applied to the edges between the breast and chest wall.

6.3.2 Clinically integrated platform

The established mechanical model of the breast has the potential to assist with the diagnosis made by clinicians on breast cancer and improve surgery planning. Further studies can also focus on the development of an application platform that combines image recruitment, image preparation, modeling, simulation, and registration. The accuracy of breast deformation simulation can be predicted by the density. Therefore, this platform can provide an overall prediction before conducting the analysis, and is more convenient for applications in clinical settings.

The images do not need to be limited to MR scans. A surface scanner can be integrated into the system, the smoothed out surface model exported from the scanner can be used as the target model, which is far more safer and faster than MR scanning. In addition, the surface scanner can be used during surgery to simultaneously complete simulation of the deformation, in order to have the most updated information on the lesion during surgery.

6.3.3 Other potential areas

AFM combined imaging

In this study, I have optimized a mechanical property, the Young's modulus, of both the adipose and fibro-glandular tissues. However, the results are taken from an inverse FEA, and thus the average value reflected by the deformation.

Atomic-force microscopes (AFM) can measure force, carry out imaging and manipulate images. When a probe is used in the AFM, it is pressed down on the object measured and according to the probe displacement and force, a stress-strain curve can be developed, which can be used to calculate the Young's modulus.

However, if an AFM is used to measure the stiffness of cells, it is difficult for the cells to survive. Even if they can be kept alive, the properties have already changed. This is because the cells are not in an in vivo environment. However, inverse FEA can measure the average stiffness of objects. A relationship between inverse FEA predicted stiffness and AFM measured stiffness might be identified by combining atomic force microscopy with inverse FEA. Therefore, a new approach that can measure the stiffness of cell and soft tissue in vivo can be developed.

References

American Cancer Society. (2014). Cancer Treatment and Survivorship Facts & Figures 2014-2015. Atlanta: American Cancer Society; 2014.

American Cancer Society. (2016a). Cancer Facts & Figures 2016. Atlanta: American Cancer Society, Atlanta: American Cancer Society; 2016.

American Cancer Society. (2016b). *Cancer Treatment & Survivorship Facts & Figures 2016-2017*.

Antoch, G., & Bockisch, A. (2009). Combined PET/MRI: a new dimension in whole-body oncology imaging? *European journal of nuclear medicine and molecular imaging, 36*(1), 113-120.

Avril, N., Rose, C., Schelling, M., Dose, J., Kuhn, W., Bense, S., Schwaiger, M. (2000). Breast imaging with positron emission tomography and fluorine-18 fluorodeoxyglucose: use and limitations. *Journal of Clinical Oncology, 18*(20), 3495-3502.

Azar, F. S., Metaxas, D. N., & Schnall, M. D. (2000). *A finite element model of the breast for predicting mechanical deformations during biopsy procedures.* Paper presented at the Mathematical Methods in Biomedical Image Analysis, 2000. Proceedings. IEEE Workshop on.

Azar, F. S., Metaxas, D. N., & Schnall, M. D. (2001). A deformable finite element model of the breast for predicting mechanical deformations under external perturbations. *Academic Radiology, 8*(10), 965-975.

Baker, L. H. (1982). Breast cancer detection demonstration project: Five‐year summary report. *CA: a cancer journal for clinicians, 32*(4), 194-225.

Bezdek, J. C. (2013). *Pattern recognition with fuzzy objective function algorithms*: Springer Science & Business Media.

Bezdek, J. C., Ehrlich, R., & Full, W. (1984). FCM: The fuzzy c-means clustering algorithm. *Computers & Geosciences, 10*(2), 191-203.

Bird, R. E., Wallace, T. W., & Yankaskas, B. C. (1992). Analysis of cancers missed at screening mammography. *Radiology, 184*(3), 613-617.

Bonet, J., & Wood, R. D. (1997). *Nonlinear continuum mechanics for finite element analysis*: Cambridge university press.

Boone, J. M., & Lindfors, K. K. (2006). Breast CT: potential for breast cancer screening and diagnosis. *Future Oncology, 2*(3), 351-356.

Brinkley, D., & Haybittle, J. (1975). The curability of breast cancer. *The Lancet, 306*(7925), 95-97.

Camacho, D. L., Hopper, R. H., Lin, G. M., & Myers, B. S. (1997). An improved method for finite element mesh generation of geometrically complex structures with application to the skullbase. *Journal of biomechanics, 30*(10), 1067-1070.

Carter, T., Tanner, C., Beechey-Newman, N., Barratt, D., & Hawkes, D. (2008). MR navigated breast surgery: method and initial clinical experience *Medical Image Computing and Computer-Assisted Intervention–MICCAI 2008* (pp. 356-363): Springer.

Cheng, H.-D., Cai, X., Chen, X., Hu, L., & Lou, X. (2003). Computer-aided detection and classification of microcalcifications in mammograms: a survey. *Pattern recognition, 36*(12), 2967-2991.

Chung, J.-H. (2008). *Modelling mammographic mechanics*.

Chung, J., Rajagopal, V., Nielsen, P., & Nash, M. (2008). A biomechanical model of mammographic compressions. *Biomechanics and modeling in mechanobiology, 7*(1), 43-52.

Ciatto, S., Houssami, N., Bernardi, D., Caumo, F., Pellegrini, M., Brunelli, S., . . . Valentini, M. (2013). Integration of 3D digital mammography with tomosynthesis for population breast-cancer screening (STORM): a prospective comparison study. *The lancet oncology, 14*(7), 583-589.

Cooper, A. P. (1840). *On the Anatomy of the Breast*: Longman.

Crum, W. R., Hartkens, T., & Hill, D. (2014). Non-rigid image registration: theory and practice. *The British journal of radiology*.

Del Palomar, A. P., Calvo, B., Herrero, J., López, J., & Doblaré, M. (2008). A finite element model to accurately predict real deformations of the breast. *Medical Engineering & Physics, 30*(9), 1089-1097.

Dufaye, G., Cherouat, A., Bachmann, J.-M., & Borouchaki, H. (2013). Advanced finite element modelling for the prediction of 3D breast deformation. *European Journal of Computational Mechanics/Revue Européenne de Mécanique Numérique, 22*(2-4), 170-182.

Dunn, J. C. (1973). A fuzzy relative of the ISODATA process and its use in detecting compact well-separated clusters.

Eiben, B., Vavourakis, V., Hipwell, J. H., Kabus, S., Buelow, T., Lorenz, C.,Hawkes, D. J. (2016). Symmetric Biomechanically Guided Prone-to-Supine Breast Image Registration. *Annals of Biomedical Engineering, 44*(1), 154-173. doi: 10.1007/s10439-015-1496-z

Ferrant, M., Nabavi, A., Macq, B., Jolesz, F. A., Kikinis, R., & Warfield, S. K. (2001). Registration of 3-D intraoperative MR images of the brain using a finite-element biomechanical model. *IEEE Transactions on Medical Imaging, 20*(12), 1384-1397.

Foskey, M., Davis, B., Goyal, L., Chang, S., Chaney, E., Strehl, N., Joshi, S. (2005). Large deformation three-dimensional image registration in image-guided radiation therapy. *Physics in Medicine and Biology, 50*(24), 5869-5892. doi: 10.1088/0031-9155/50/24/008

Fung, Y.-c., & Tong, P. (2001). *Classical and computational solid mechanics* (Vol. 1): World scientific.

Gamage, T. P. B., Boyes, R., Rajagopal, V., Nielsen, P. M., & Nash, M. P. (2012). Modelling prone to supine breast deformation under gravity loading using heterogeneous finite element models *Computational Biomechanics for Medicine* (pp. 29-38): Springer.

Gamage, T. P. B., Rajagopal, V., Nielsen, P. M., & Nash, M. P. (2011). Patient-specific modeling of breast biomechanics with applications to breast cancer detection and treatment *Patient-Specific Modeling in Tomorrow's Medicine* (pp. 379-412): Springer.

Gefen, A., & Dilmoney, B. (2007). Mechanics of the normal woman's breast. *Technol Health Care, 15*(4), 259-271.

Gennisson, J.-L., Baldeweck, T., Tanter, M., Catheline, S., Fink, M., Sandrin, L., . . . Querleux, B. (2004). Assessment of elastic parameters of human skin using dynamic elastography. *IEEE transactions on ultrasonics, ferroelectrics, and frequency control, 51*(8), 980-989.

Giger, M. L. (2000). Computer‐Aided Diagnosis of Breast Lesions in Medical Images. *Computing in Science & Engineering, 2*(5), 39-45.

Guldberg, R., Hollister, S., & Charras, G. (1998). The accuracy of digital image-based finite element models. *Journal of Biomechanical Engineering, 120*(2), 289-295.

Guo, Y., Sivaramakrishna, R., Lu, C.-C., Suri, J. S., & Laxminarayan, S. (2006). Breast image registration techniques: a survey. *Medical and Biological Engineering and Computing, 44*(1-2), 15-26.

Haberkorn, U., & Schoenberg, S. O. (2001). Imaging of lung cancer with CT, MRT and PET. *Lung Cancer, 34*, 13-23.

Hall, M., Frank, E., Holmes, G., Pfahringer, B., Reutemann, P., & Witten, I. H. (2009). The WEKA data mining software: an update. *ACM SIGKDD explorations newsletter, 11*(1), 10-18.

Hale, S. (2014). How Do I Know If My Mesh is Good Enough? , from https://caeai.com/blog/how-do-i-know-if-my-mesh-good-enough, accessed by 20/12/2016

Han, L., Hipwell, J. H., Eiben, B., Barratt, D., Modat, M., Ourselin, S., & Hawkes, D. J. (2014). A nonlinear biomechanical model based registration method for aligning prone and supine mr breast images. *Medical Imaging, IEEE Transactions on, 33*(3), 682-694.

Han, L. H., Hipwell, J. H., Tanner, C., Taylor, Z., Mertzanidou, T., Cardoso, J., Hawkes, D. J. (2012). Development of patient-specific biomechanical models for predicting large breast deformation. *Physics in Medicine and Biology, 57*(2), 455-472. doi: Doi 10.1088/0031-9155/57/2/455

Harper, A. P., Kelly-Fry, E., & Noe, J. S. (1981). Ultrasound breast imaging—the method of choice for examining the young patient. *Ultrasound in medicine & biology, 7*(3), 231-237.

Hawkes, D. (1998). Algorithms for radiological image registration and their clinical application. *Journal of Anatomy, 193*(3), 347-361.

Hibbett, Karlsson, & Sorensen. (1998). *ABAQUS/standard: User's Manual* (Vol. 1): Hibbitt, Karlsson & Sorensen.

Hill, D. L., Batchelor, P. G., Holden, M., & Hawkes, D. J. (2001). Medical image registration. *Physics in Medicine and Biology, 46*(3), R1.

Hill, D. L., Hawkes, D. J., Crossman, J., Gleeson, M., Cox, T., Bracey, E.,Graves, P. (1991). Registration of MR and CT images for skull base surgery using point-like anatomical features. *The British journal of radiology, 64*(767), 1030-1035.

Hopp, T., Dietzel, M., Baltzer, P. A., Kreisel, P., Kaiser, W. A., Gemmeke, H., & Ruiter, N. V. (2013). Automatic multimodal 2D/3D breast image registration using biomechanical FEM models and intensity-based optimization. *Medical image analysis, 17*(2), 209-218.

Humphrey, J., & Rajagopal, K. (2002). A constrained mixture model for growth and remodeling of soft tissues. *Mathematical models and methods in applied sciences, 12*(03), 407-430.

International commission on radiological protection, (2009). Adult reference computational phantoms, *ICRP Publication 110, Ann. ICRP 39 (2)*, pp.48-51 Table A.1.

Jackson, V. P., Hendrick, R. E., Feig, S. A., & Kopans, D. B. (1993). Imaging of the radiographically dense breast. *Radiology, 188*(2), 297-301.

Kagadis, G. C., & Langer, S. G. (2011). *Informatics in medical imaging*: CRC Press.

Kato, Z., & Pong, T.-C. (2006). A Markov random field image segmentation model for color textured images. *Image and Vision Computing, 24*(10), 1103-1114.

Keyak, J., Fourkas, M., Meagher, J., & Skinner, H. (1993). Validation of an automated method of three-dimensional finite element modelling of bone. *Journal of Biomedical Engineering, 15*(6), 505-509.

Krol, A., Unlu, M. Z., Magri, A., Lipson, E., Coman, I. L., Mandel, J. A.,Feiglin, D. H. (2006). *Iterative finite element deformable model for nonrigid coregistration of multimodal breast images.* Paper presented at the Biomedical Imaging: Nano to Macro, 2006. 3rd IEEE International Symposium on.

Krouskop, T. A., Wheeler, T. M., Kallel, F., Garra, B. S., & Hall, T. (1998). Elastic moduli of breast and prostate tissues under compression. *Ultrasonic imaging, 20*(4), 260-274.

Kuhlmann, M., Fear, E., Ramirez-Serrano, A., & Federico, S. (2013). Mechanical model of the breast for the prediction of deformation during imaging. *Medical Engineering & Physics, 35*(4), 470-478.

L'Etang, A., & Huang, Z. (2006). FE simulation of laser generated surface acoustic wave propagation in skin. *Ultrasonics, 44*, e1243-e1247.

Lapuebla-Ferri, A., del Palomar, A. P., Herrero, J., & Jiménez-Mocholí, A.-J. (2011). A patient-specific FE-based methodology to simulate prosthesis insertion during an augmentation mammoplasty. *Medical Engineering & Physics, 33*(9), 1094-1102.

Lee, A. W., Schnabel, J. A., Rajagopal, V., Nielsen, P. M., & Nash, M. P. (2010). Breast image registration by combining finite elements and free-form deformations *Digital Mammography* (pp. 736-743): Springer.

Li, C., Guan, G., Reif, R., Huang, Z., & Wang, R. K. (2012). Determining elastic properties of skin by measuring surface waves from an impulse mechanical stimulus using phase-sensitive optical coherence tomography. *Journal of The Royal Society Interface, 9*(70), 831-841.

Li, S. Z. (2009). *Markov random field modeling in image analysis*: Springer Science & Business Media.

Liang, X., & Boppart, S. A. (2010). Biomechanical properties of in vivo human skin from dynamic optical coherence elastography. *Ieee Transactions on Biomedical Engineering, 57*(4), 953-959.

Liu, C., Yuen, J., & Torralba, A. (2011). Sift flow: Dense correspondence across scenes and its applications. *Pattern Analysis and Machine Intelligence, IEEE Transactions on, 33*(5), 978-994.

Lorensen, W. E., & Cline, H. E. (1987). *Marching cubes: A high resolution 3D surface construction algorithm.* Paper presented at the ACM siggraph computer graphics.

Marks, L., & Gardner, T. (1993). The use of strain energy as a convergence criterion in the finite element modelling of bone and the effect of model geometry on stress convergence. *Journal of Biomedical Engineering, 15*(6), 474-476.

Martel, A., Froh, M., Brock, K., Plewes, D., & Barber, D. (2007). Evaluating an optical-flow-based registration algorithm for contrast-enhanced magnetic resonance imaging of the breast. *Physics in Medicine and Biology, 52*(13), 3803.

Mendez, A., Cabanillas, F., Echenique, M., Malekshamran, K., Perez, I., & Ramos, E. (2004). Evaluation of Breast Imaging Reporting and Data System Category 3 mammograms and the use of stereotactic vacuum‐assisted breast biopsy in a nonacademic community practice. *Cancer, 100*(4), 710-714.

Mohamed, A., & Davatzikos, C. (2004). *Finite element mesh generation and remeshing from segmented medical images.* Paper presented at the Biomedical Imaging: Nano to Macro, 2004. IEEE International Symposium on.

Moskowitz, M. (1995). Breast imaging. *Cancer of the Breast. New York: Saunders*, 206-239.

Moy, L., Ponzo, F., Noz, M. E., Maguire, G. Q., Murphy-Walcott, A. D., Deans, A. E., Kramer, E. L. (2007). Improving specificity of breast MRI using prone PET and fused MRI and PET 3D volume datasets. *Journal of Nuclear Medicine, 48*(4), 528-537.

Müller, R., & Rüegsegger, P. (1995). Three-dimensional finite element modelling of non-invasively assessed trabecular bone structures. *Medical Engineering & Physics, 17*(2), 126-133.

Mushlin, A. I., Kouides, R. W., & Shapiro, D. E. (1998). Estimating the accuracy of screening mammography: a meta-analysis. *American journal of preventive medicine, 14*(2), 143-153.

New World Encyclopedia. (2008). Mammary Gland. Retrieved 2016.5.1, from http://www.newworldencyclopedia.org/entry/Mammary_gland)

Nie, K., Su, M.-Y., Chau, M.-K., Chan, S., Nguyen, H., Tseng, T., . . . Chen, J.-H. (2010). Age-and race-dependence of the fibroglandular breast density analyzed on 3D MRI. *Medical physics, 37*(6), 2770-2776.

Orel, S. G., & Schnall, M. D. (2001). MR imaging of the breast for the detection, diagnosis, and staging of breast cancer 1. *Radiology, 220*(1), 13-30.

Palomar, P., Calvo, B., Herrero, J., López, J., & Doblaré, M. (2008). A finite element model to accurately predict real deformations of the breast. *Medical Engineering & Physics, 30*(9), 1089-1097.

Pathmanathan, P., Gavaghan, D., Whiteley, J., Brady, M., Nash, M., Nielsen, P., & Rajagopal, V. (2004). Predicting tumour location by simulating large deformations of the breast using a 3D finite element model and nonlinear elasticity *Medical Image Computing and Computer-Assisted Intervention–MICCAI 2004* (pp. 217-224): Springer.

Pathmanathan, P., Gavaghan, D. J., Whiteley, J. P., Chapman, S. J., & Brady, J. M. (2008). Predicting Tumor Location by Modeling the Deformation of the Breast. *Ieee Transactions on Biomedical Engineering, 55*(10), 2471-2480. doi: 10.1109/tbme.2008.925714

Phelps, M. E. (2000). Positron emission tomography provides molecular imaging of biological processes. *Proceedings of the National Academy of Sciences, 97*(16), 9226-9233.

Picard, R. R., & Cook, R. D. (1984). Cross-validation of regression models. *Journal of the American Statistical Association, 79*(387), 575-583.

Qiu, Y., Li, L., Goldgof, D., Sarkar, S., Anton, S., & Clark, R. A. (2004). *Three-dimensional finite element model for lesion correspondence in breast imaging.* Paper presented at the Medical Imaging 2004.

Quinlan, J. R. (2014). *C4. 5: programs for machine learning*: Elsevier.

Rajagopal, V. (2007). *Modelling breast tissue mechanics under gravity loading.* Citeseer.

Rajagopal, V., Chung, J., Nielsen, P., & Nash, M. (2006). *Finite element modelling of breast biomechanics: Finding a reference state.* Paper presented at the

Engineering in Medicine and Biology Society, 2005. IEEE-EMBS 2005. 27th Annual International Conference of the.

Rajagopal, V., Lee, A., Chung, J.-H., Warren, R., Highnam, R. P., Nash, M. P., & Nielsen, P. M. (2008). Creating individual-specific biomechanical models of the breast for medical image analysis. *Academic Radiology, 15*(11), 1425-1436.

Ramos, A., & Simoes, J. (2006). Tetrahedral versus hexahedral finite elements in numerical modelling of the proximal femur. *Medical Engineering & Physics, 28*(9), 916-924.

Richard, F. J., Bakic, P. R., & Maidment, A. D. (2006). Mammogram registration: a phantom-based evaluation of compressed breast thickness variation effects. *IEEE Transactions on Medical Imaging, 25*(2), 188-197.

Rieber, A., Schirrmeister, H., Gabelmann, A., Nuessle, K., Reske, S., Kreienberg, R., Kuehn, T. (2002). Pre-operative staging of invasive breast cancer with MR mammography and/or PET: boon or bunk? *The British journal of radiology, 75*(898), 789-798.

Roose, L., De Maerteleire, W., Mollemans, W., & Suetens, P. (2005). *Validation of different soft tissue simulation methods for breast augmentation.* Paper presented at the International Congress Series.

Roose, L., Mollemans, W., Loeckx, D., Maes, F., & Suetens, P. (2006). *Biomechanically based elastic breast registration using mass tensor simulation.* Paper presented at the International Conference on Medical Image Computing and Computer-Assisted Intervention.

Säbel, M., & Aichinger, H. (1996). Recent developments in breast imaging. *Physics in Medicine and Biology, 41*(3), 315.

Samani, A., Bishop, J., Yaffe, M. J., & Plewes, D. B. (2001). Biomechanical 3-D finite element modeling of the human breast using MRI data. *Medical Imaging, IEEE Transactions on, 20*(4), 271-279.

Samani, A., & Plewes, D. (2004). A method to measure the hyperelastic parameters of ex vivo breast tissue samples. *Physics in Medicine and Biology, 49*(18), 4395.

Samani, A., Zubovits, J., & Plewes, D. (2007). Elastic moduli of normal and pathological human breast tissues: an inversion-technique-based investigation of 169 samples. *Physics in Medicine and Biology, 52*(6), 1565.

Sarrut, D. (2006). Deformable registration for image-guided radiation therapy. *Zeitschrift für medizinische Physik, 16*(4), 285-297.

Schnabel, J. A., Tanner, C., Smith, A. D. C., Hill, D. L., Hawkes, D. J., Leach, M. O.,Hose, R. (2001). *Validation of non-rigid registration using finite element methods.* Paper presented at the Biennial International Conference on Information Processing in Medical Imaging.

Sermesant, M., Delingette, H., & Ayache, N. (2006). An electromechanical model of the heart for image analysis and simulation. *IEEE Transactions on Medical Imaging, 25*(5), 612-625.

Smith, R. A., Duffy, S. W., Gabe, R., Tabar, L., Yen, A. M., & Chen, T. H. (2004). The randomized trials of breast cancer screening: what have we learned? *Radiologic Clinics of North America, 42*(5), 793-806.

Solis, S., Rodriguez, A., & Tomasi, D. (2010). *Study of the magnetic interaction of a 4-coil array and copper shielding with a PET/MRI using the finite-element method.* Paper presented at the 2010 Annual International Conference of the IEEE Engineering in Medicine and Biology.

Studholme, C., Hill, D. L., & Hawkes, D. J. (1996). Automated 3-D registration of MR and CT images of the head. *Medical image analysis, 1*(2), 163-175.

Studholme, C., Hill, D. L., & Hawkes, D. J. (1997). Automated three-dimensional registration of magnetic resonance and positron emission tomography brain images by multiresolution optimization of voxel similarity measures. *Medical physics, 24*(1), 25-35.

Sullivan, J. M., Charron, G., & Paulsen, K. D. (1997). A three-dimensional mesh generator for arbitrary multiple material domains. *Finite Elements in Analysis and Design, 25*(3), 219-241.

Tang, C., Zhang, G., & Tsui, C. (2009). A 3D skeletal muscle model coupled with active contraction of muscle fibres and hyperelastic behaviour. *Journal of biomechanics, 42*(7), 865-872.

Tanner, C., Schnabel, J. A., Hill, D. L., Hawkes, D. J., Leach, M. O., & Hose, D. R. (2006). Factors influencing the accuracy of biomechanical breast models. *Medical physics, 33*(6), 1758-1769.

University of Cambridge/Department of Engineering. (2002). Young's Modulus-Density.from http://www.materials.eng.cam.ac.uk/mpsite/interactive_charts/stiffness-density/basic.html. Accessed: 3rd August 2016.

Unlu, M. Z., Król, A., Magri, A., Mandel, J. A., Lee, W., Baum, K. G.,Feiglin, D. H. (2010). Computerized method for nonrigid MR-to-PET breast-image registration. *Computers in biology and medicine, 40*(1), 37-53.

Viceconti, M., Bellingeri, L., Cristofolini, L., & Toni, A. (1998). A comparative study on different methods of automatic mesh generation of human femurs. *Medical Engineering & Physics, 20*(1), 1-10.

Walter, C., Scheidhauer, K., Scharl, A., Goering, U.-J., Theissen, P., Kugel, H., Pietrzyk, U. (2003). Clinical and diagnostic value of preoperative MR mammography and FDG-PET in suspicious breast lesions. *European radiology, 13*(7), 1651-1656.

Wellman, P., Howe, R. D., Dalton, E., & Kern, K. A. (1999). Breast tissue stiffness in compression is correlated to histological diagnosis. *Harvard BioRobotics Laboratory Technical Report*, 1-15.

Wellman, P. S., Dalton, E. P., Krag, D., Kern, K. A., & Howe, R. D. (2001). Tactile imaging of breast masses: first clinical report. *Archives of surgery, 136*(2), 204-208.

Wendler, T., Herrmann, K., Schnelzer, A., Lasser, T., Traub, J., Kutter, O.,Kiechle, M. (2010). First demonstration of 3-D lymphatic mapping in breast cancer using freehand SPECT. *European journal of nuclear medicine and molecular imaging, 37*(8), 1452-1461.

Wu, W.-J., & Moon, W. K. (2008). Ultrasound breast tumor image computer-aided diagnosis with texture and morphological features. *Academic Radiology, 15*(7), 873-880.

Xu, F., Wen, T., Lu, T., & Seffen, K. (2008). Skin biothermomechanics for medical treatments. *Journal of the Mechanical Behavior of Biomedical Materials, 1*(2), 172-187.

Zhang, Y., Qiu, Y., Goldgof, D. B., Sarkar, S., & Li, L. (2007). *3D finite element modeling of nonrigid breast deformation for feature registration in-ray and MR images.* Paper presented at the Applications of Computer Vision, 2007. WACV'07. IEEE Workshop on.

Zhong, Y.-j., & Chen, L.-Z. (2014). *A Novel Algorithm Based on SIFT and Graph Transformation for Mammogram Registration.* Paper presented at the Proceedings of the 2012 International Conference on Cybernetics and Informatics.

Zienkiewicz, O. C., Taylor, R. L., Zienkiewicz, O. C., & Taylor, R. L. (1977). *The finite element method* (Vol. 3): McGraw-hill London.